Construction and Building Materials 520 (2026) 146009

Contents lists available at ScienceDirect

Construction and Building Materials

journal homepage: www.elsevier.com/locate/conbuildmat

Residual performance of lime, cementitious, and alkali-activated TRM systems after high temperature exposure

Daniele Berdini [a], Alessandra Mobili [a,*], Gianluca Chiappini [b], Valeria Corinaldesi [a], Jacopo Donnini [a]

[a] Department of Science and Engineering of Matter, Environment and Urban Planning, Marche Polytechnic University, via Brecce Bianche 12, Ancona 60131, Italy
[b] Department of Theoretical and Applied Sciences, eCampus University, via Isimbardi 10, Novedrate 22060, Italy

ARTICLE INFO

Keywords:
Textile Reinforced Mortar
Alkali-Activated Mortar
TRM
TRAAM
Basalt Textile
Fly Ash
Metakaolin
Lime
Temperature
Mechanical Performance

ABSTRACT

Textile Reinforced Mortar (TRM) composite systems have recently been developed using environmentally sustainable binders, including alkali-activated mortars (AAMs). Despite their promising mechanical performance and reduced environmental impact, the feasibility of incorporating AAMs into TRM strengthening systems has not yet been fully established. In particular, the behaviour of AAM-based TRM composites, known as TRAAMs, under elevated temperatures remains poorly understood, and limited experimental evidence is currently available regarding their mechanical stability, bond performance, and failure mechanisms after thermal exposure. This study investigates and compares the performance of TRM systems manufactured with different binders (lime, cement, and alkali-activated) reinforced with coated basalt textiles, both at room temperature (20 °C) and after exposure to elevated temperatures (200 °C, 400 °C, and 600 °C). Residual properties were assessed through mechanical testing and microstructural analyses. Furthermore, the results were benchmarked against data available in the literature for comparable TRM systems subjected to high temperatures. The findings indicate that exposure up to 200 °C has a negligible influence on the TRM residual performance, with TRAAM systems even showing slight improvements. Conversely, exposure to 400 °C and above leads to a significant degradation of performance in all TRM systems.

1. Introduction

Textile Reinforced Mortar (TRM), also referred to as Fabric Reinforced Cementitious Matrix (FRCM), has emerged as a promising alternative to conventional strengthening techniques for the rehabilitation and retrofitting of existing structures [1–3]. This system consists of a textile reinforcement, typically arranged as a bidirectional grid of carbon, basalt, or glass fibers, embedded within an inorganic matrix and externally bonded to structural elements. Its effectiveness has been extensively demonstrated and validated through numerous experimental studies on both masonry [4–8] and reinforced concrete [9–12] elements.

Traditionally, the inorganic matrices used in TRM systems are based on lime or Portland cement. However, in response to increasing sustainability requirements and the global transition toward low-carbon construction, both research and industry have focused on alternative binders capable of delivering comparable or superior mechanical and durability performance, such as blended cements combining multiple supplementary cementitious materials (SCMs) [13] or alkali-activated binders [14]. In this context, alkali-activated mortars (AAMs) have attracted growing research interest as potential substitutes for conventional lime- or cement-based matrices. AAMs can provide substantial reductions in CO_2 emissions, typically ranging between 30% and 80% compared to traditional mortars [15]. The magnitude of this reduction depends strongly on the precursor employed (commonly industrial by-products such as fly ash or blast furnace slag, and natural calcined clays such as metakaolin), as well as on the type and concentration of the alkaline activator (e.g., silicates, hydroxides, carbonates, or sulfates) [16]. Beyond their environmental advantages, AAMs have also shown promising mechanical performance and durability characteristics, making them attractive candidates for sustainable TRM applications [17–19].

Recent studies have further demonstrated the feasibility of using AAMs as matrices in TRM or FRCM systems, commonly referred to as

* Corresponding author.
E-mail address: a.mobili@staff.univpm.it (A. Mobili).

https://doi.org/10.1016/j.conbuildmat.2026.146009
Received 19 January 2026; Received in revised form 21 February 2026; Accepted 16 March 2026
Available online 20 March 2026
0950-0618/© 2026 The Authors. Published by Elsevier Ltd. This is an open access article under the CC BY license (http://creativecommons.org/licenses/by/4.0/).

TRAAMs, showing that they can achieve comparable or even superior mechanical performance, bond behavior, and durability compared to traditional lime- or cement-based matrices when used to strengthen masonry and concrete structures [20–22]. Preliminary evidence also suggests that TRAAMs may retain higher residual mechanical capacity and bond strength than their cementitious counterparts after elevated temperature exposure, indicating potential advantages in fire or high-temperature scenarios [22]. Despite the inorganic nature of TRM matrices, which often leads to the perception of inherent fire resistance, both lime- and cement-based TRMs remain susceptible to thermal degradation that compromises mechanical performance and bond effectiveness at elevated temperatures [23–25]. Tetta and Bournas [26] studied the thermal behavior of both FRP and TRM systems up to 250 °C, showing that TRMs retained shear resistance more effectively than FRPs: the shear strength of TRM decreased by 36% after exposure to 250 °C, whereas FRP strength dropped by 88% already at 150 °C. Maroudas and Papanicolaou [27] studied AR-glass TRMs exposed to elevated temperature and observed a temperature-dependent failure mode: fibre slippage up to 100 °C, and strip debonding and fibre rupture at 200–300 °C. Askouni et al. [28] investigated normal weight and lightweight TRM systems with AR-glass textile at room temperature, 120 °C, and 200 °C. After exposure to 120 °C both systems exhibited similar bond capacity, whereas at 200 °C lightweight TRMs showed lower resistance, with maximum textile axial stress reductions of 50% and 36% for single- and double-layer overlays, respectively. Increasing matrix thickness was also found beneficial for residual bond capacity. The same authors [29] compared cement-based and metakaolin/fly-ash alkali-activated TRMs exposed to 200 °C and 400 °C, reporting that at 400 °C all systems retained approximately 50% of their original shear bond strength, while TRAAMs outperformed cement-based counterparts at both temperatures. Moreover, the exposure did not modify the failure mode, which remained governed by sleeve fibre rupture combined with core fibre slippage. Assessing the residual behavior of TRMs after thermal exposure is therefore essential to ensure the safety and durability of reinforced structures. Residual strength after high-temperature exposure, depends on multiple parameters, including the type of fiber, the nature of the matrix, and the fiber coating [30]. In general, higher thermal stability of the matrix is associated with improved residual performance after heating [31]. However, polymer-based coatings may decompose at temperatures around 400 °C, causing deterioration of the fibre–matrix bond [32]. Indeed, Estevan et al. [31] reported that, in systems with polymer-coated textiles, clear signs of degradation become evident after exposure to 400 °C, which was identified as the primary cause of strength loss in TRM systems. In addition to textile degradation, matrix deterioration plays a significant role in the mechanical response of TRM systems, as reduced adhesion at the fibre–matrix interface directly compromises load transfer between the two constituents. In the study by Estevan et al. [31], two types of hydraulic lime-based mortars were used as matrices; the formulation containing synthetic polymers in water dispersion retained less mechanical strength after heating, due to the degradation of polymers already at approximately 200 °C. For cement-based matrices, exposure to elevated temperatures induces significant chemical and microstructural changes, including dehydration of calcium silicate hydrate (C-S-H) gel at around 150 °C, dehydroxylation of calcium hydroxide (CH) near 450 °C, the α to β quartz phase transition at approximately 570 °C, and decarbonation of calcium carbonate ($CaCO_3$) around 700 °C [18]. These transformations, combined with thermally induced gradients, generate microcracking during heating and cooling cycles, further impairing mechanical performance.

Basalt fibre, produced by melting basalt rock at temperatures between 1500 °C and 1700 °C, represents a cost-effective and sustainable reinforcement material [33]. It exhibits favourable mechanical properties for strengthening applications in both masonry [34] and concrete elements [35].

Nevertheless, the high-temperature behaviour of basalt-reinforced TRAAM systems incorporating alkali-activated binders remains insufficiently investigated. Li et al. [36] produced slag-based TRAAM panels with hybrid basalt/steel fiber and studied their flexural behavior after exposure to high temperatures (400 °C, 600 °C, and 800 °C). The panels exhibited deflection-hardening behaviour, although flexural performance progressively decreased with increasing temperature and exposure duration due to matrix decomposition and phase transformations that weakened the fibre-matrix bond. Tamburini et al. [37] investigated a metakaolin/slag alkali-activated grout used to bond basalt, glass, carbon textiles, and steel cord fabrics to clay bricks. The matrix showed good chemical and physical stability, compressive strength of approximately 45 MPa after 28 days, and satisfactory strength retention after exposure to 200 °C, 400 °C, and 600 °C. Overall, previous studies have mainly focused on slag-based AAMs, and direct comparisons between TRAAMs and traditional lime- and cement-based TRMs remain limited. To address this gap, the present study systematically investigates the thermal performance of lime, cement, and two alkali-activated TRM systems based on metakaolin and fly ash, reinforced with a coated basalt textile. Mechanical, physical, and microstructural assessments were carried out up to 600 °C, using SEM, TGA, and XRD analyses to correlate residual mechanical behavior with microstructural evolution and to clarify the degradation mechanisms governing TRM failure at elevated temperatures. The study also identifies temperature thresholds and degradation modes specific to each binder, providing new insight for the design of thermally resilient TRM systems.

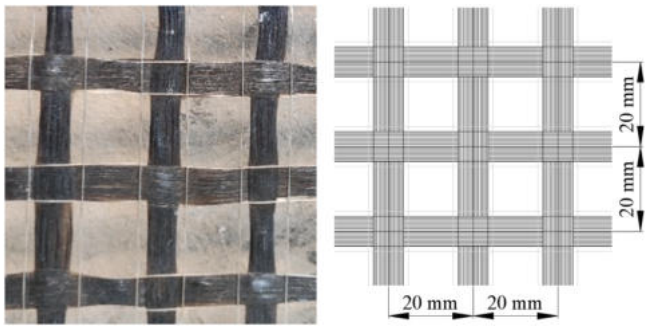


Fig. 1. Bidirectional basalt textile employed as TRM reinforcement.

Table 1
Geometrical and mechanical properties of the basalt textile (from manufacturer technical data sheet).

Material	Dry Textile weight (g/m^2)	Coated Textile weight (g/m^2)	Basalt density (g/cm^3)	Cross-sectional area of single yarn (mm^2)	Textile resistant area (mm^2/m)	Textile tensile strength (kN/m)
Basalt textile (B)	365	420	2.70	1.33	66.67	132

2. Experimental procedures

2.1. Materials

2.1.1. Basalt textile

A commercial bidirectional basalt textile (Glasstex Struktura BA 420 provided by Biemme S.r.l.), pre-impregnated with a polyester-based coating, was employed as the TRM reinforcement (Fig. 1). The geometrical and mechanical properties of the textile at room temperature, as provided by the manufacturer, are reported in Table 1. In addition, basalt yarns were characterized through tensile tests after exposure to elevated temperatures (see Section 2.2.2).

Table 2
Mix proportions of alkali-activated mortars (g/L) and flow value (mm).

Mixture	Sand	Mixing water	Premixed mortar	FA	MKK	Activators			w/b*	w/s**	Flow value
						SS	KOH	Water			
FAK	1375	20	-	468	-	153	61	92	0.33	-	153
MKK	1066	47	-	-	395	237	63	174	0.63	-	168
CEM	-	312	1697	-	-	-	-	-	-	0.18	131
LIME	-	303	1428	-	-	-	-	-	-	0.21	118

* w/b = water/binder ratio (in FAK and MKK the binder is the sum of FA, MK and solids dissolved in SS and KOH)
** w/s = water/solid ratio (in CEM and LIME the solid is the sum of binders and aggregates)

2.1.2. Alkali-activated mortars

Two types of AAMs were designed and produced using different aluminosilicate precursors. The first, referred to as FAK, is based on class F fly ash (FA), supplied by General Admixture S.p.A., while the second, denoted MKK, is based on Metastar® 501 metakaolin (MK), produced by Imerys Minerals Ltd. The FA exhibited a specific surface area (SSA) of 5000 cm^2/g and an average particle diameter of 20 μm. In contrast, the MK had a much higher SSA of 140000 cm^2/g, corresponding to very fine particles with an average diameter of 3 μm. A calcareous sand characterized by a maximum particle size of 3 mm and a water absorption capacity of 3.4% by mass, as determined according to EN 1097–6 [38], was employed. The activating solution consisted of a mixture of sodium silicate (SS), supplied by Ingessil S.r.l., with a SiO_2/Na_2O molar ratio of 2:1, and potassium hydroxide (KOH). One day prior to casting, the alkaline activators were prepared and premixed to allow proper cooling and to promote the polymerization reaction with the aluminosilicate precursors. On the casting day, the dry powders were first mixed for 2 min; the activator was then added and mixed for an additional 3 min together with extra water required to achieve the desired workability. The mix proportions of the AAMs were adopted and adjusted from previous studies [39], based on their 28-day compressive strength (approximately 10 MPa for the metakaolin-based AAM and greater than 30 MPa for the fly ash-based AAM), and are reported in Table 2.

2.1.3. Lime and cement-based mortars

Two commercial premixed mortars were also investigated: i) a lime-based mortar (LIME), classified as strength class R1 (i.e., 28-day compressive strength between 10 and 15 MPa, according to EN 1504–3 [40]), formulated with natural hydraulic lime (NHL 3.5) and sand with a maximum particle size of 1.4 mm; and ii) a cement-based mortar (CEM), classified as strength class R4 (i.e., 28-day compressive strength exceeding 45 MPa, according to EN 1504–3 [40]), containing aggregates with a maximum particle size of 0.5 mm. These commercial mortars served as reference mixtures for the two innovative AAMs: the properties of the MKK mortar were compared with those of LIME, while the properties of the FAK mortar were compared with those of CEM.

2.2. Methods

2.2.1. Physical-mechanical characterization of mortars

The consistency of the fresh mortar was assessed using a flow table test in accordance with EN 1015–3 [41], with results expressed as the mean spread diameter after 15 jolts. Mortar prisms (40 × 40 × 160 mm^3) were cast and cured for 28 days under laboratory conditions (20 ± 2 °C and relative humidity (RH) of 65 ± 5%) prior to compression and flexural tests, in accordance with EN 1015–11 [42].

In addition, the dynamic modulus of elasticity was evaluated using a PUNDIT ultrasonic device with a resolution of 0.1 μs, in accordance with EN 12504–4 [43]. This method relates the dynamic modulus of elasticity (E_d), to the hardened density (ρ) of the specimen, and the velocity of ultrasonic waves (v) transmitted along the specimen length at a frequency of 50 kHz, as expressed in Eq. (1). In this equation, γ_d denotes Poisson's modulus, assumed to be 0.20 for all mortars, and k is a constant dependent on γ_d.

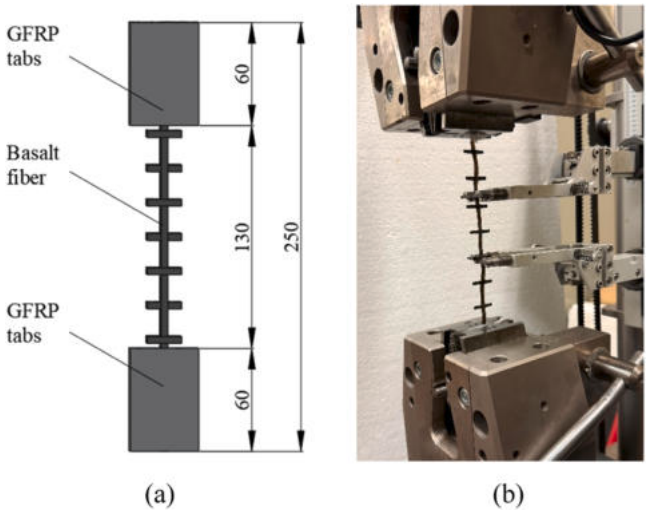


Fig. 2. Tensile test on basalt yarn: (a) specimen geometry and dimensions (in mm), (b) test setup.

$$E_d = k \bullet \rho \bullet v^2, \quad \text{with} \quad k = \frac{(1+\gamma_d)(1-2\gamma_d)}{(1-\gamma_d)} \tag{1}$$

For each mortar type and exposure temperature, three 40 × 40 × 160 mm^3 specimens were manufactured. All mortars were cured under standard laboratory conditions for 90 days before being subjected to thermal exposures of 200 °C, 400 °C, and 600 °C.

2.2.2. Tensile tests on basalt yarns

The effect of elevated temperatures on residual performance of basalt yarns was evaluated through a series of tensile tests. Yarns were exposed to 200 °C, 400 °C, and 600 °C for 120 min prior to testing. For each exposure condition, four yarn specimens were tested, along with unexposed samples that served as reference. The geometry of the specimens and the tensile test configuration are shown in Fig. 2. All tests were conducted in accordance with the Italian guideline for the identification, qualification, and acceptance of inorganic matrix fiber-reinforced composites (FRCM) [44] using a Zwick Z050 universal testing machine with a maximum load capacity of 50 kN. The tests were performed under displacement control at a constant crosshead speed of 0.5 mm/min. Prior to testing, GFRP tabs were bonded to both ends of each specimen. The tabs consisted of two layers of quadriaxial glass fabric laminated with a two-component epoxy resin. The tab dimensions were 60 mm in length, 40 mm in width, and 2 mm in thickness. Wedge grips were used to grab the specimen (Fig. 2b).

The tensile strength (σ_{yarn}) was determined by dividing the maximum applied load (F) by the cross-sectional area of a single yarn (A_y), measured as 1.33 mm^2 (from manufacturer). The strain was measured by using a macro-extensometer with a gauge length of 50 mm directly applied to the surface of the yarn. The elastic modulus (E_{yarn}) was calculated as the secant modulus in the load interval ranging from

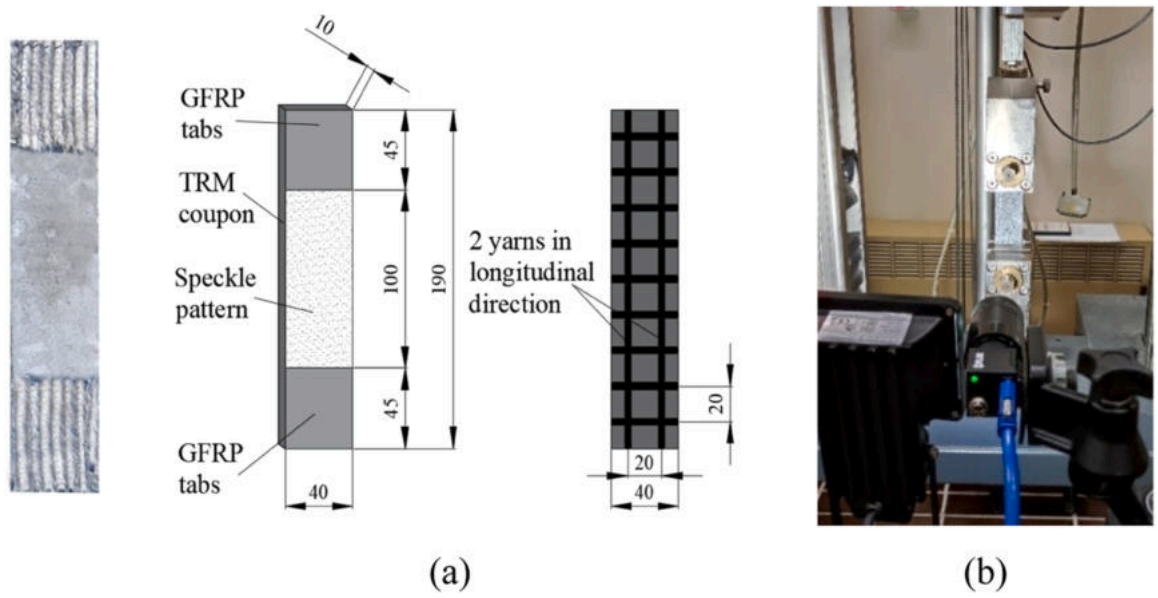


Fig. 3. Tensile test on TRM coupon: (a) specimen geometry and dimensions in mm, (b) test setup with DIC acquisition system.

Table 3
Settings of the stereo-DIC.

CMOS cameras	FLIR Blackfly S BFS-U3-88S6M-C
Lens	Fujinon CF50ZA-1S
Image resolution	4096 × 2160 pixels, 8 bit
Field of view	170 × 90 mm
Pixel to mm conversion	1 pixel = 0.0415 mm
Stereo-angle	16°
Stand-off distance	700 mm
Patterning technique	Matt white spray paint base coat with black speckles
DIC technique	Stereo correlation
DIC software	MatchID, version 2024.1
Image filtering Gaussian	Gaussian, 5 × 5 pixel kernel
Subset size	21 × 21
Step size	5 px
Matching criterion	Zero-normalized sum of square differences (ZNSSD)
Interpolant	Bi-cubic spline
Stereo transformation	Affine
Strain computation	Gradient

1/10–1/2 of the maximum load, following the UNI EN 2561 standard [45].

These tests were specifically designed to assess the residual tensile strength of coated basalt yarns after exposure to high temperatures. The results also provide a basis for interpreting tensile tests on TRM coupons, offering valuable information on the potential ability of the mortar matrix to protect the internal reinforcement.

2.2.3. Tensile tests on TRM coupons

Prismatic TRM coupons measuring 190 × 40 × 10 mm^3 were fabricated to evaluate the residual tensile strength after high temperature exposure, by varying the type of inorganic matrix. Due to the limited dimensions of the furnace, the typical TRM specimen dimensions (usually 500 mm of length) as prescribed by current regulations, could not be adopted. The 10 mm-thick mortar layer was reinforced with a basalt textile consisting of two yarns aligned in the longitudinal direction. TRM coupons were cured for 28 days at laboratory conditions (20 ± 2 °C, 65 ± 5% RH) prior to thermal conditioning. To ensure effective load transfer and to prevent premature failure at the grips during tensile testing, GFRP tabs (45 × 40 mm^2) were epoxy-bonded to the ends of each coupon. The test setup is shown in Fig. 3. Tensile tests were performed under displacement control at a rate of 0.5 mm/min using a Zwick Z050 universal testing machine with a maximum load capacity of 50 kN. Digital Image Correlation (DIC) was employed to monitor axial strain and crack propagation throughout the tests. Images were captured using two digital cameras (FLIR Blackfly S BFS-U3–88S6M-C model) equipped with 50 mm focal length lenses (Fujinon CF50ZA-1S), synchronized with the testing machine force measurements. During the tests, images of the specimen gauge section were captured after applying a speckle pattern to the surface using spray paint. The image sequence was then analyzed using a DIC algorithm implemented in the commercial software MatchID (https://www.matchid.eu), based on a subset-based DIC formulation. A subset size of 21 × 21 pixels and a step size of 5 pixels were adopted. The complete stereo-DIC configuration is summarized in Table 3. Displacement and strain maps were evaluated within a rectangular region of interest (ROI) corresponding to the front face of the specimen. The resulting data were subsequently processed using custom MATLAB scripts to compute the axial strain and generate the corresponding stress-strain curves. Furthermore, the full-field strain measurements were used to identify surface cracking patterns and to monitor their evolution over time during testing. Tensile stress (σ) was calculated by dividing the applied tensile load (F) by the total cross-sectional area of the textile (2.66 mm^2). The tensile stress corresponding to the formation of the first crack within the matrix is reported as $\sigma_{1,TRM}$ while the tensile strength is denoted as $\sigma_{max,TRM}$. The TRM tensile strength was then compared to the tensile strength of the bare textile at room temperature (20 °C), to determine the exploitation ratio. The average elastic modulus in the post-cracking phase ($E_{2,TRM}$) was evaluated graphically as the slope of the stress-strain curve after first cracking.

2.2.4. High temperature conditioning protocol

All samples, including basalt yarns, mortar prisms, and TRM coupons, were exposed to temperatures of 200 °C, 400 °C, and 600 °C. For mortar prims and TRM coupons, thermal conditioning was performed after 90 days of curing under laboratory conditions (T = 20 ± 2 °C, RH = 65 ± 5%). Specimens were placed in the furnace at room temperature, after which the temperature was increased at a rate of 10 °C/min (as for the study of the microstructural changes performed by thermogravimetric analysis, see Section 2.2.5). Once the target temperature was reached, it was maintained for 2 h, after which the samples were allowed to cool naturally in the switched-off furnace for 24 h. The duration of exposure was chosen based on previous studies investigating the high temperature behavior of TRM systems [22,32,46].

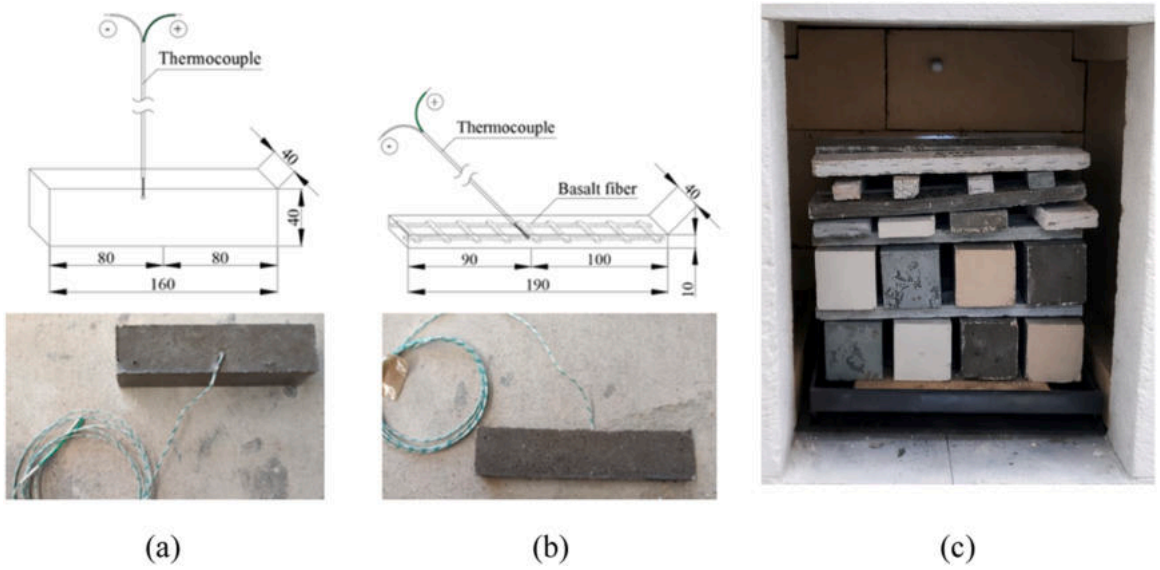


Fig. 4. Position of thermocouples: (a) inside the mortar prism and (b) at the textile-to-matrix interface in TRM coupons (dimensions are in mm). (c) Arrangement of specimens inside the furnace.

The temperature at the textile-to-mortar interface in TRM coupons and within the mortar prisms was monitored throughout the conditioning process using K-type thermocouples (Figs. 4a and 4b) connected to a Keysight DAQ970A data acquisition system. The sensors were directly embedded into the matrices in the fresh state during specimen preparation. The positioning of the specimens inside the furnace is shown in Fig. 4c.

2.2.5. Microstructural analyses

To evaluate the behavior of different matrices at elevated temperatures, thermogravimetric analysis (TGA) was performed on paste samples ground and sieved to 100 μm using a SII EXSTAR TG/DTA 6200. The samples were heated from room temperature to 1000 °C at a rate of 10 °C/min in an oxidizing atmosphere (air).

To investigate the pore structure, a fragment of each mortar after each exposure temperature was analyzed by mercury intrusion porosimetry (MIP) using a Thermo Fisher 240 Pascal with (pressure range 0.1–200 MPa) and a Thermo Fisher 140 Pascal (pressure range 0.1–400 kPa).

X-ray diffraction (XRD) analysis was conducted on powdered mortar samples (with particle size lower than 90 μm) at 20 °C and after each thermal exposure using a Bruker AXS D8 Advance diffractometer/reflectometer.

Microstructural analysis was carried out on graphite-coated fragments with a PHILIPS XL20 scanning electron microscope (SEM).

3. Results and discussion

3.1. Consistency of fresh mortar

As reported in Table 2, both FAK and MKK exhibited slightly higher flow values (>150 mm) compared to lime- and cement-based mortars, which showed flow values below 135 mm. The higher flow observed in the FAK mortar is attributed to the spherical morphology of fly ash particles, which reduces internal friction and improves workability [47]. On the other hand, the increased flow of the MKK mortar is associated

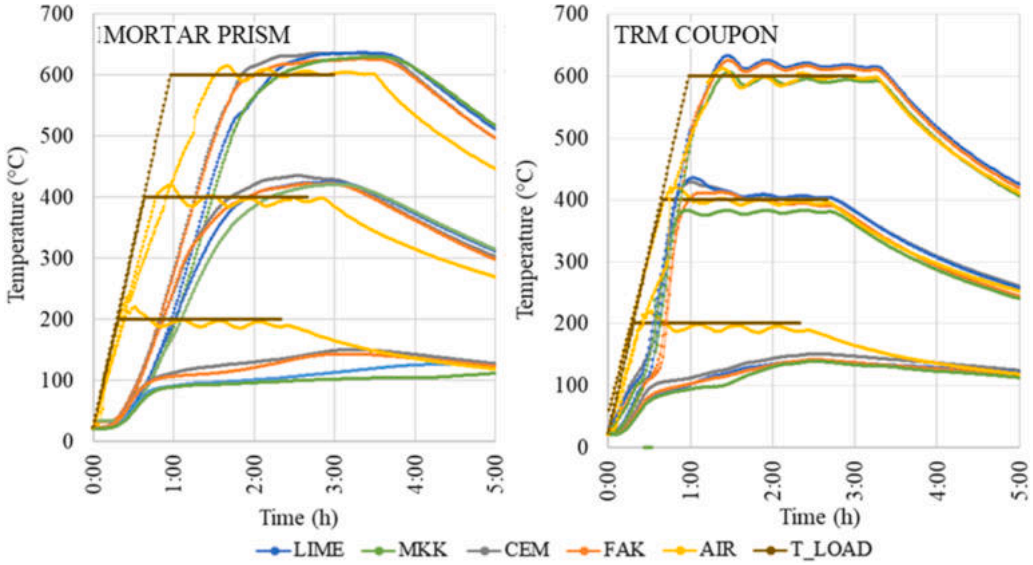


Fig. 5. Temperature profiles of mortar prisms and TRM coupons exposed to 200 °C, 400 °C, and 600 °C.

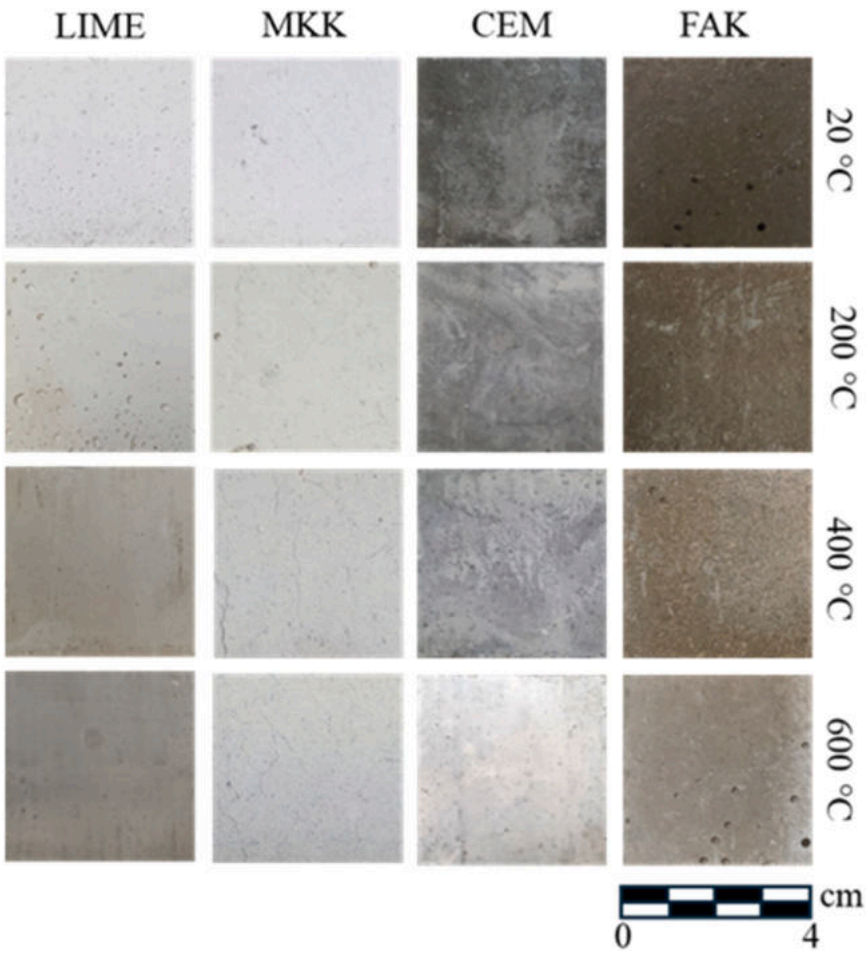


Fig. 6. Surface appearance of mortars after exposure to 20 °C, 200 °C, 400 °C, and 600 °C.



Fig. 7. Cracked LIME sample (left) and warped MKK TRM coupon (right), both after 600 °C exposure.

with its high water content, which is necessary to ensure proper dispersion of metakaolin particles as a result of their high specific surface area (SSA) [48].

3.2. Effects of high temperature exposure on mortars and TRM

The results of the temperature measurements recorded by thermocouples embedded within the mortar specimens and TRM coupons are

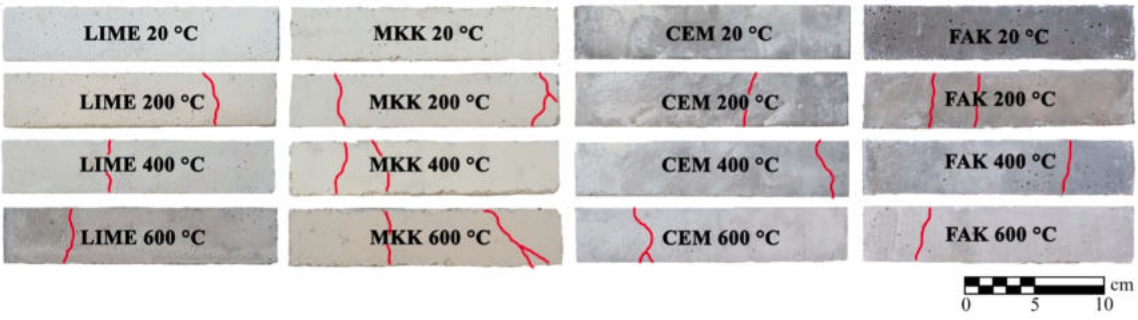


Fig. 8. TRM coupons after exposure to 20 °C, 200 °C, 400 °C, and 600 °C.

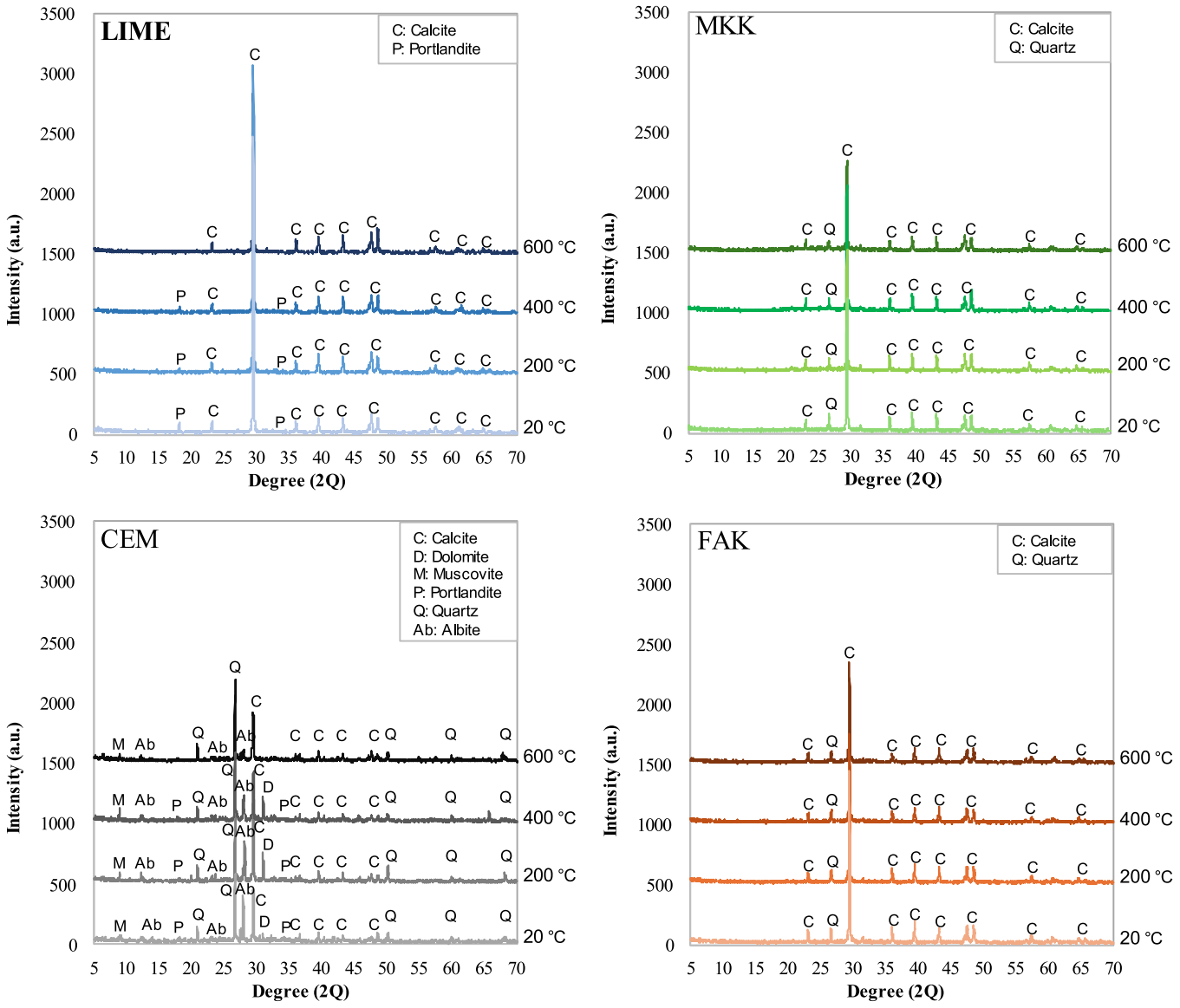


Fig. 9. XRD patterns of mortars after exposure to 20, 200, 400 and 600 °C.

presented in Fig. 5. T_LOAD denotes the temperature set in the furnace, while AIR refers to the temperature measured by a thermocouple positioned at the center of the furnace. It is worth noting that, after two hours of exposure, the target temperature was reached in the specimens subjected to 400 °C and 600 °C. In contrast, for specimens exposed to 200 °C, the internal temperature remained below the furnace setpoint. In this case, the temperature recorded inside the mortar prisms reached approximately 150 °C for the CEM and FAK mortars, whereas lower values, in the range of 100–120 °C, were measured for the LIME and MKK mortars. For the TRM coupons, the temperature measured at the textile-to-mortar interface after two hours of exposure at 200 °C was approximately 140–150 °C. Regarding the heating rate within the specimens, higher temperature increase rates were observed for the CEM and FAK specimens, while slightly lower rates characterized the LIME and MKK specimens.

FAK and CEM mortars exhibited progressive discoloration (fading) as a result of dehydration, whereas the LIME mortars darkened, as shown in Fig. 6, where the color changes of mortars after each exposure temperature are displayed. Regarding structural integrity (Fig. 7a), visible cracking in mortar prisms was observed only after exposure to 600 °C. In contrast, TRM coupons cracked already at 200 °C (Fig. 8). This behavior can be attributed to the slenderness of the samples and to the evaporation of the pore water induced by rapid heating [49]. MKK mortar specimens largely retained their original color (Fig. 6) but exhibited the most pronounced warping (bowing) in the TRM coupons (Figs. 7b and 8). This response is likely related to the higher water content of the MKK specimens combined with the lower stiffness of the material, which promoted bowing during drying.

3.3. XRD

XRD analyses of mortars heated at different temperatures are presented in Fig. 9. At room temperature (20 °C), LIME mortars were primarily composed of portlandite ($Ca(OH)_2$) and calcite ($CaCO_3$); CEM mortars consisted of portlandite, calcite, quartz (SiO_2), muscovite ($KAl_2(AlSi_3O_{10})(F,OH)_2$), albite ($NaAlSi_3O_8$), and dolomite ($CaMg(CO_3)_2$). In contrast, both FAK and MKK mortars were mainly composed of calcite and quartz. The pronounced calcite peaks observed in all mortars are primarily attributed to the calcareous sand used as aggregate, whereas the remaining phases reflect the specific binder compositions. For both LIME and CEM mortars, the mineralogical composition remained largely unchanged with increasing temperature up to 400 °C. At 600 °C,

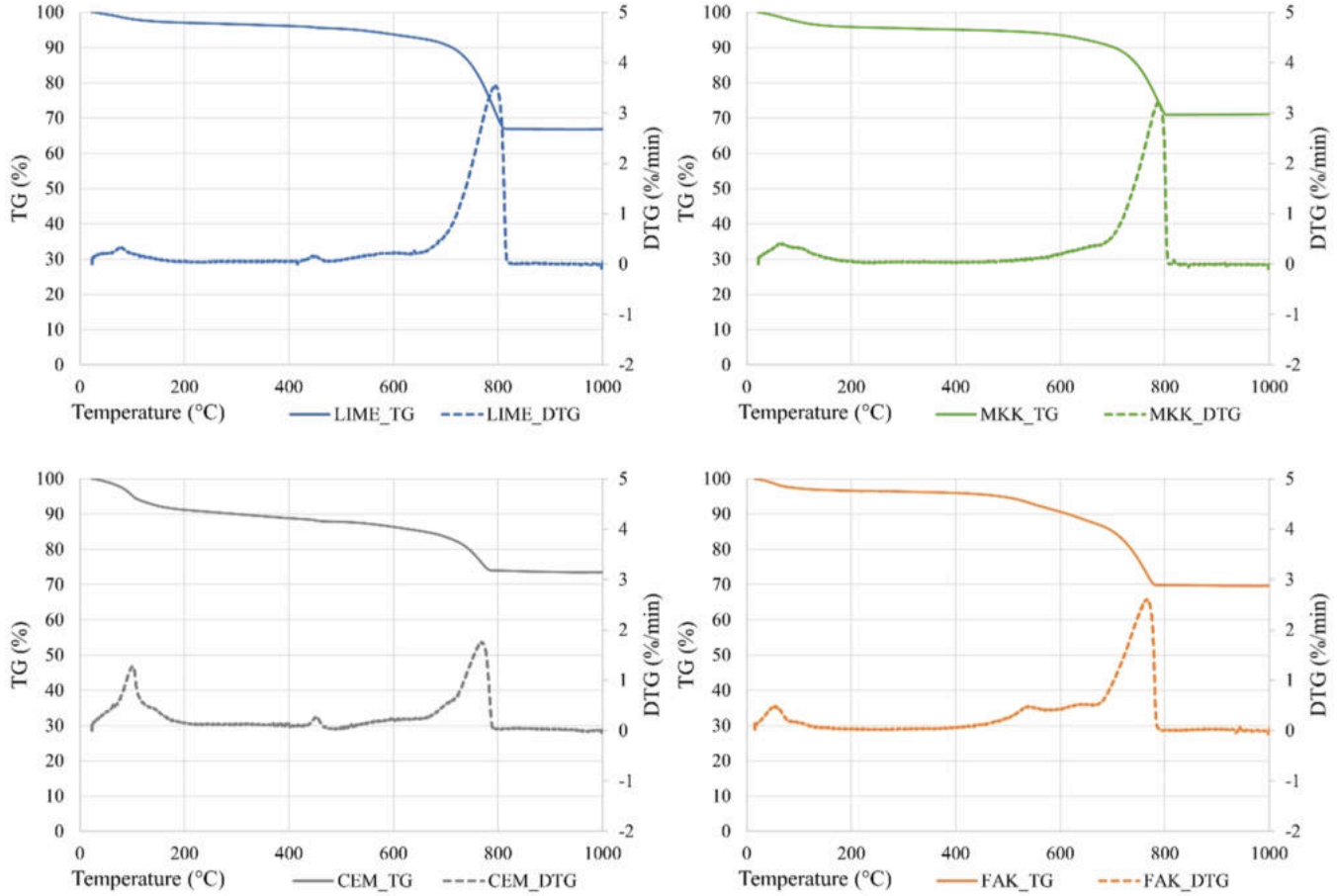


Fig. 10. TG-DTG curves of mortars heated up to 1000 °C in air.

however, portlandite peaks disappeared, consistent with its decomposition into lime (CaO) and water vapor, which typically occurs between 450 °C and 550 °C [50]. In CEM mortars, the dolomite peak also vanished after heating to 600 °C, in agreement with literature reporting the onset of dolomite decomposition at approximately 500 °C [51]. AAMs based on fly ash (FAK) and metakaolin (MKK) showed good thermal stability, showing no microstructural changes up to 600 °C. As reported by Zhang et al. [52], both 100% metakaolin- and fly ash-based AAMs exhibit mass losses up to 300 °C due to evaporation of free and bound water, while no significant loss occurs between 500 °C and 800 °C. [50]. Accordingly, quartz and calcite peaks were detected in all samples throughout the investigated temperature range (20–600 °C). During heating, quartz undergoes polymorphic transformations; however, under the investigated conditions (ambient pressure and temperature up to 600 °C), only the α-quartz to β-quartz transition was observed, occurring at approximately 573 °C [53]. Calcite decomposition initiates at around 600 °C and is completed near 850 °C, with the formation of CaO and the release of CO_2 [54].

3.4. TGA

The TG-DTG curves of mortars tested from room temperature (20 °C) up to 1000 °C are shown in Fig. 10. Overall, all mortars exhibited an initial mass loss between 200 °C and 300 °C. In LIME and CEM mortars, this loss is mainly associated with the evaporation of free water. In FAK and MKK mortars, the mass loss reduction is primarily attributed to the evaporation of both free water and chemically bound water within the alkali-activated matrix [52]. This loss was relatively limited in most mortars (approximately 3–4%), except for the CEM mortar, which showed the highest mass loss (around 10%) [18]. The evaporation of free water does not alter the chemical phases present in the paste, as it only involves physical changes in the matrix, mainly related to an increase in total porosity and/or pore size [55]. In LIME and CEM mortars, an additional minor mass loss was observed around 420 °C, corresponding to the initial dehydroxylation of $Ca(OH)_2$ into CaO and water [50,18], and visible in the DTG curves where a small peak arises. Subsequently, all mortars experienced a major mass loss at approximately 600 °C, attributed to the decomposition of the calcareous aggregate (primarily $CaCO_3$) into lime (CaO) and CO_2 [54]. Moreover, in the FAK mortar an additional peak in the DTG curve was detected above 550 °C, corresponding to the α-quartz to β-quartz transformation [53], given the high quartz content of the fly ash precursor. No further significant mass losses were detected in any mortar between 800 °C and 1000 °C. By the end of the test, all mortars exhibited an overall mass reduction of approximately 30%. A strong correlation between TG and XRD analyses is evident, as the temperature-dependent mass-loss trends are consistent with the phase transformations identified by XRD test (Fig. 9).

3.5. SEM

Fig. 11 presents the SEM images of TRM specimen cross-sections after exposure to the different temperatures. The observations that can be made on the degradation of the basalt yarn coated with polyester-based resin are valid for all the systems observed, regardless of the type of mortar used. At 200 °C, the basalt fibers remain well embedded within the polymer, with some debonding observed at the interfacial transition zone (ITZ) between yarn and matrix interface, especially in the MKK, CEM, and FAK specimens. However, the polymer coating does not appear to have undergone any alterations. This indicates that such a temperature is insufficient to degrade the thermosetting polymer,

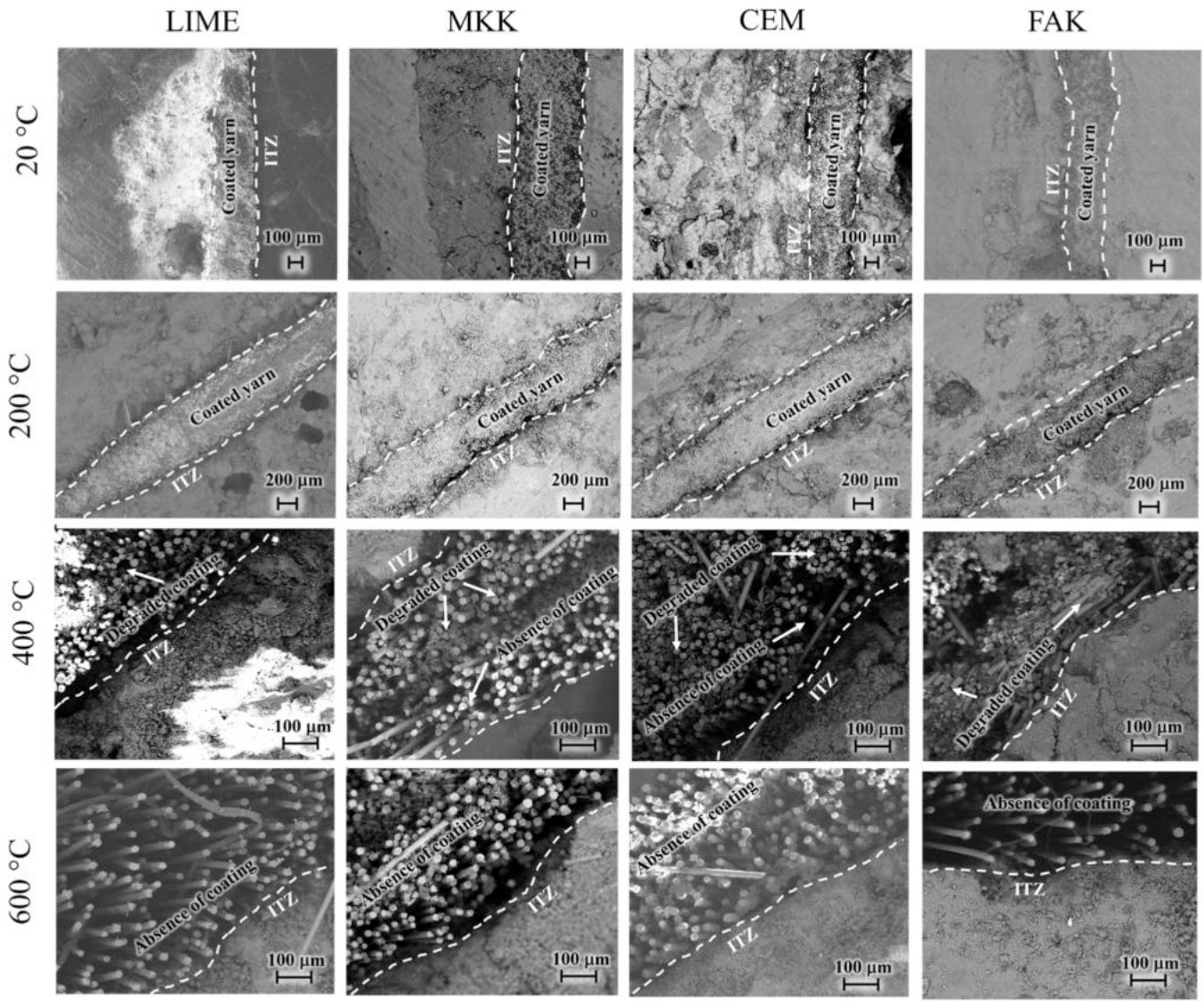


Fig. 11. SEM images of TRM specimen cross-sections after exposure to 20, 200, 400 and 600 °C.

Table 4
Mechanical and physical properties of matrices after high temperature exposure, COV in round brackets.

Matrix	Flexural strength R_f (MPa)	Compressive strength R_c (MPa)	Dynamic modulus of elasticity E_d (GPa)	Hardened density ρ (kg/m^3)
LIME_20	3.8 (1%)	12.2 (6%)	12.2 (2%)	1707 (1%)
LIME_200	4.2 (23%)	10.9 (4%)	7.7 (7%)	1535 (1%)
LIME_400	2.9 (4%)	8.2 (7%)	5.5 (1%)	1520 (1%)
LIME_600	0.3 (11%)	2.7 (21%)	2.2 (6%)	1490 (1%)
MKK_20	1.8 (10%)	8.6 (4%)	6.4 (26%)	2020 (2%)
MKK_200	2.4 (40%)	9.8 (4%)	5.7 (23%)	1656 (2%)
MKK_400	1.2 (12%)	8.4 (4%)	3.1 (5%)	1568 (1%)
MKK_600	0.9 (2%)	7.8 (10%)	2.0 (33%)	1561 (1%)
CEM_20	10.5 (3%)	56.6 (7%)	30.2 (1%)	2036 (1%)
CEM_200	9.8 (14%)	42.3 (3%)	18.7 (3%)	1848 (1%)
CEM_400	4.5 (11%)	31.2 (2%)	11.5 (4%)	1736 (1%)
CEM_600	2.6 (10%)	19.5 (11%)	5.4 (6%)	1736 (1%)
FAK_20	8.6 (3%)	52.6 (6%)	38.8 (1%)	2298 (1%)
FAK_200	7.3 (35%)	67.6 (10%)	23.5 (16%)	2187 (1%)
FAK_400	3.0 (25%)	29.9 (13%)	10.0 (23%)	2172 (1%)
FAK_600	2.1 (11%)	23.4 (11%)	6.1 (13%)	2053 (3%)

which, upon cooling, continues to effectively bond the individual basalt filaments together. When the exposure temperature increases to 400 °C, some voids begin to appear between the filaments and at the yarn/inorganic matrix interface, evidencing significant degradation of the polymer coating. At 600 °C, the coating is completely decomposed, as shown by the presence of uncoated basalt filaments within the matrix. These microstructural observations are consistent with and substantiate the results obtained from the tensile tests on TRM coupons.

3.6. Mechanical tests

Results of mortar characterization tests in terms of flexural strength (R_f), compressive strength (R_c), dynamic modulus of elasticity (E_d), and hardened density (ρ) are reported in Table 4.

After 28 days of curing at room temperature, LIME and MKK mortars showed comparable mechanical properties, with flexural and compressive strengths of approximately 2–4 and 9–12 MPa, respectively, with LIME consistently exhibiting slightly higher values than MKK (Fig. 12). Similarly, CEM and FAK mortars displayed comparable strength levels, with flexural strengths of around 11–12 MPa and compressive strength of 53–57 MPa (Figs. 12 and 13).

Following exposure to 200 °C, the flexural and compressive strengths

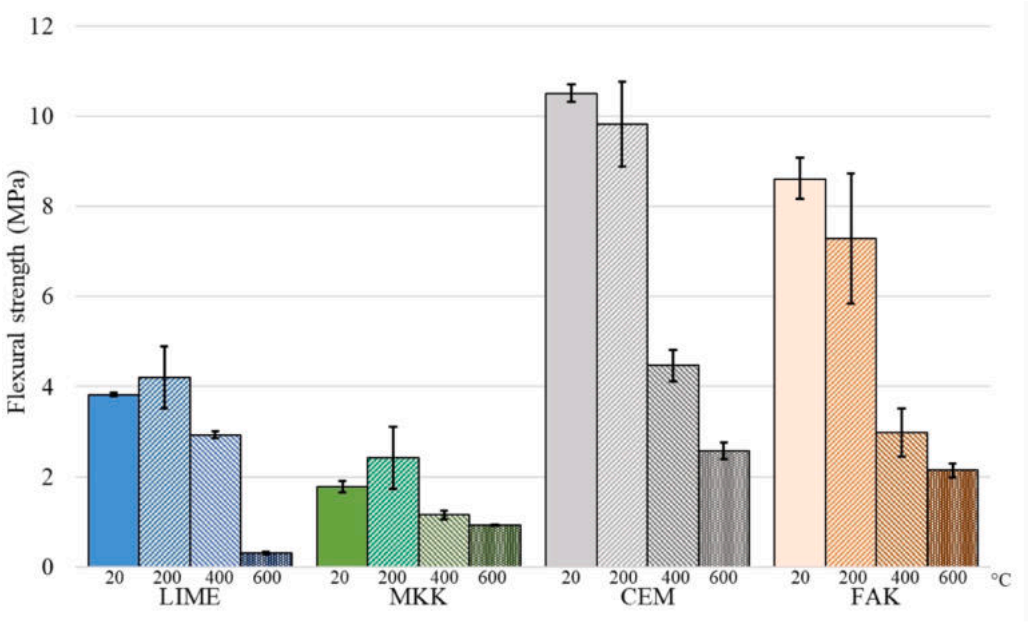


Fig. 12. Flexural strength of mortars after exposure to 20 °C, 200 °C, 400 °C, and 600 °C.

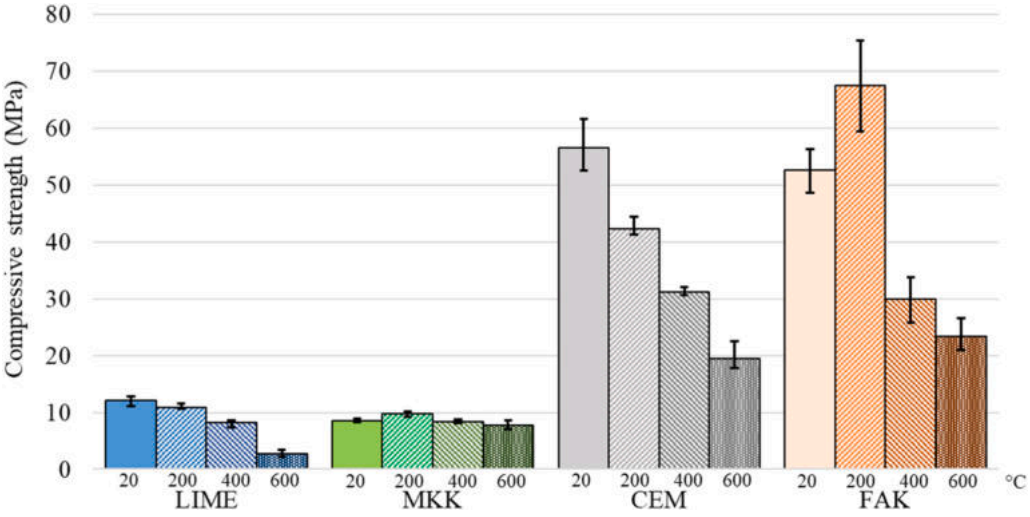


Fig. 13. Compressive strength of mortars after exposure to 20 °C, 200 °C, 400 °C, and 600 °C.

of LIME mortar remained almost unchanged. Although total porosity slightly increased (Fig. 14), the pore size distribution remained largely unaffected (Fig. 15). Further temperature increases to 400 °C and 600 °C, however, resulted in a marked reduction in mechanical performance. This degradation is attributed to the decomposition of portlandite into lime and water vapor [50,18], as previously discussed. The release of water vapor under pressure causes rupture of the pore walls and the formation of microcracks [56]. In contrast, the MKK mortar exhibited a slight increase in mechanical properties after exposure to 200 °C and only a limited reduction in compressive strength (<10%) up to 600 °C.

CEM and FAK mortars exhibited distinct behavior at 200 °C. While CEM mortar experienced a reduction of approximately 25% in compressive strength, FAK mortar showed an increase of about 29% (Fig. 13). These contrasting trends can be explained by their different microstructural evolutions. In CEM mortar, total porosity increased from 12% to 19% and pore diameters became larger (Fig. 15). In contrast, FAK mortar exhibited a nearly unchanged pore size distribution (Fig. 15), along with a slight decrease in total porosity from 16% to 13% (Fig. 14).

Fly ash- and metakaolin-based alkali-activated mortars are characterized by a three-dimensional alkali aluminosilicate hydrate (N-A-S-H) gel structure [57], which can be regarded as a zeolite precursor, consisting of silicon tetrahedra linked to aluminum tetrahedra and charge-balanced by Na^+ ions. At approximately 200 °C, water associated with this structure (zeolitic water) evaporates without affecting the integrity of the aluminosilicate framework or its dimensional stability [56]. Cao et al. [58] reported that the strength increase observed in AAMs after exposure to 200 °C can be attributed to dehydration and polymerization of the silicate network, leading to the formation of a more robust O–Si–O structure at around 120 °C. This mechanism explains the increase in compressive strength observed for both FAK and MKK mortars at 200 °C. On the other hand, the reduction in flexural strength of the FAK matrix may be attributed to the formation of microcracks after exposure to 200 °C, likely induced matrix embrittlement. However, this result exhibits considerable variability and should be confirmed through additional experimental investigations.

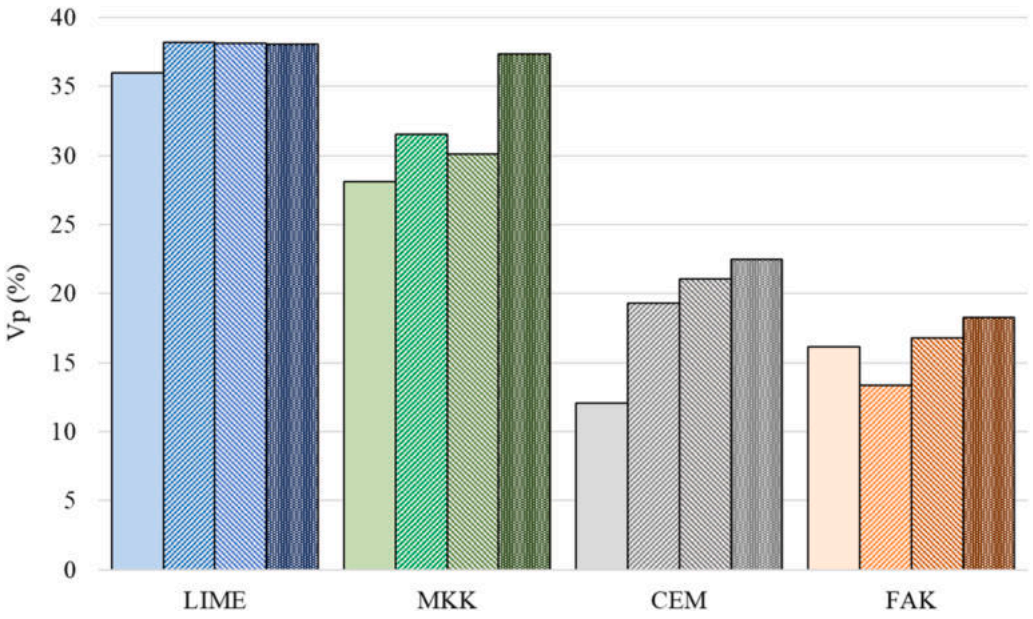


Fig. 14. Total porosity of mortars after exposure to 20 °C, 200 °C, 400 °C, and 600 °C.

At higher temperatures, both CEM and FAK mortars exhibited significant strength degradation, with compressive strength losses of approximately 43% at 400 °C and over 55% at 600 °C (Fig. 13), with a slight decrease in total porosity from 16% to 13% (Fig. 14). Beyond 400 °C, fly ash- and metakaolin-based AAMs may undergo irreversible dehydration, during which alkali ions (Na^+) migrate into the oxygen framework previously associated with hydrogen in water molecules, leading to shrinkage of the system [56]. In CEM mortars, shrinkage begins between 300 °C and 400 °C as water evaporates from the C–S–H gel. Further temperature increases induce portlandite decomposition, water vapor expansion within the pores, and extensive microcracking. The resulting internal pressure significantly reduces compressive strength and may ultimately lead to structural failure [59].

The microstructural evolution of CEM and FAK mortars observed in this study is consistent with the literature findings, showing a progressive increase in total porosity with rising temperature and a shift in pore size distribution toward larger diameters. The dynamic modulus of elasticity (E_d) decreased progressively with increasing temperature for all mortar types (Fig. 16), regardless of the trend observed in mechanical strength. At 200 °C, the evaporation of free water reduced material density (Fig. 17), and since density and modulus are directly proportional (see Eq. (1)), E_d values also decreased. This reduction became more pronounced at 400 °C and 600 °C, where structural degradation and loss of mechanical integrity further contributed to the decrease of stiffness.

3.7. Tensile tests on basalt yarns

Results of tensile tests on single basalt yarns after exposure to different temperatures are reported in Table 5. At room temperature (20 °C), the average tensile strength of the basalt yarns was 1346 MPa. After exposure to 200 °C, the tensile strength remained largely unchanged, with an average value of 1306 MPa, corresponding to only a marginal reduction compared to the reference condition. In contrast, a pronounced decrease in tensile strength was observed at 400 °C, where the average tensile stress dropped sharply to 278 MPa, representing approximately 21% of the original strength. This substantial reduction reflects severe fiber degradation accompanied by deterioration of the external coating. These findings are consistent with prior SEM analyses, which revealed extensive microstructural damage at this temperature. Furthermore, these results are fully consistent with what was observed by Rambo et al. [49] and Yang and Krevaikas [60] on similar basalt textiles. At 600 °C, the specimens exhibited an average tensile stress of only 44 MPa, indicating an almost complete loss of load-bearing capacity. Visual inspection further confirmed thermally induced changes in the polymeric coating. Fibers exposed to 200 °C retained their overall geometry but became noticeably harder and more brittle than the reference specimens, consistent with melting followed by re-solidification of the coating. This modification precedes the temperature range (250–400 °C) at which the polyester coating [61] and basalt fiber sizing [62] typically degrade. From 400 °C onward, the basalt filaments showed severe fraying and loss of cohesion, indicative of complete decomposition of the polyester-based coating.

3.8. Tensile tests on TRM coupons

The parameters calculated for each TRM system are summarized in Table 6 as average values obtained from two or three specimens per exposure temperature, with the corresponding COV reported in brackets. The tensile test results are also presented in the form of stress–strain curves in Fig. 19, while the strain distribution and crack patterns are shown in Fig. 20. TRM coupons exhibit the typical tensile response that can be approximated as bilinear or trilinear.

The first cracking stress ($\sigma_{1,TRM}$) is primarily dependent on the mechanical properties of the inorganic matrix. This parameter is determined for all TRM systems up to an exposure temperature of 200 °C. At higher temperatures (400 °C and 600 °C), $\sigma_{1,TRM}$ could not be reliably identified, as the matrices exhibited pre-existing cracks or microcracks, often not visible to the naked eye, induced by thermal conditioning.

At room temperature (20 °C), the CEM-TRM systems showed the highest tensile strength, followed in descending order by LIME, FAK, and MKK systems. The modulus of elasticity in the cracked phase ($E_{2,TRM}$) exhibited the same trend, indicating that cement- and lime-based matrices provide greater stiffness to TRM systems compared to alkaline-activated matrices. The relatively lower modulus observed in TRAAM systems is likely associated to reduced adhesion at the textile-to-matrix interface in TRM composites incorporating alkaline-activated binders. After exposure to 200 °C, a slight reduction in tensile strength is observed for all TRM systems, except for the metakaolin-based system, which instead exhibited an increase in tensile strength. Specifically, the tensile strength reductions were approximately 5%, 10%, and 19% for the LIME, CEM, and FAK systems, respectively, whereas the MKK system

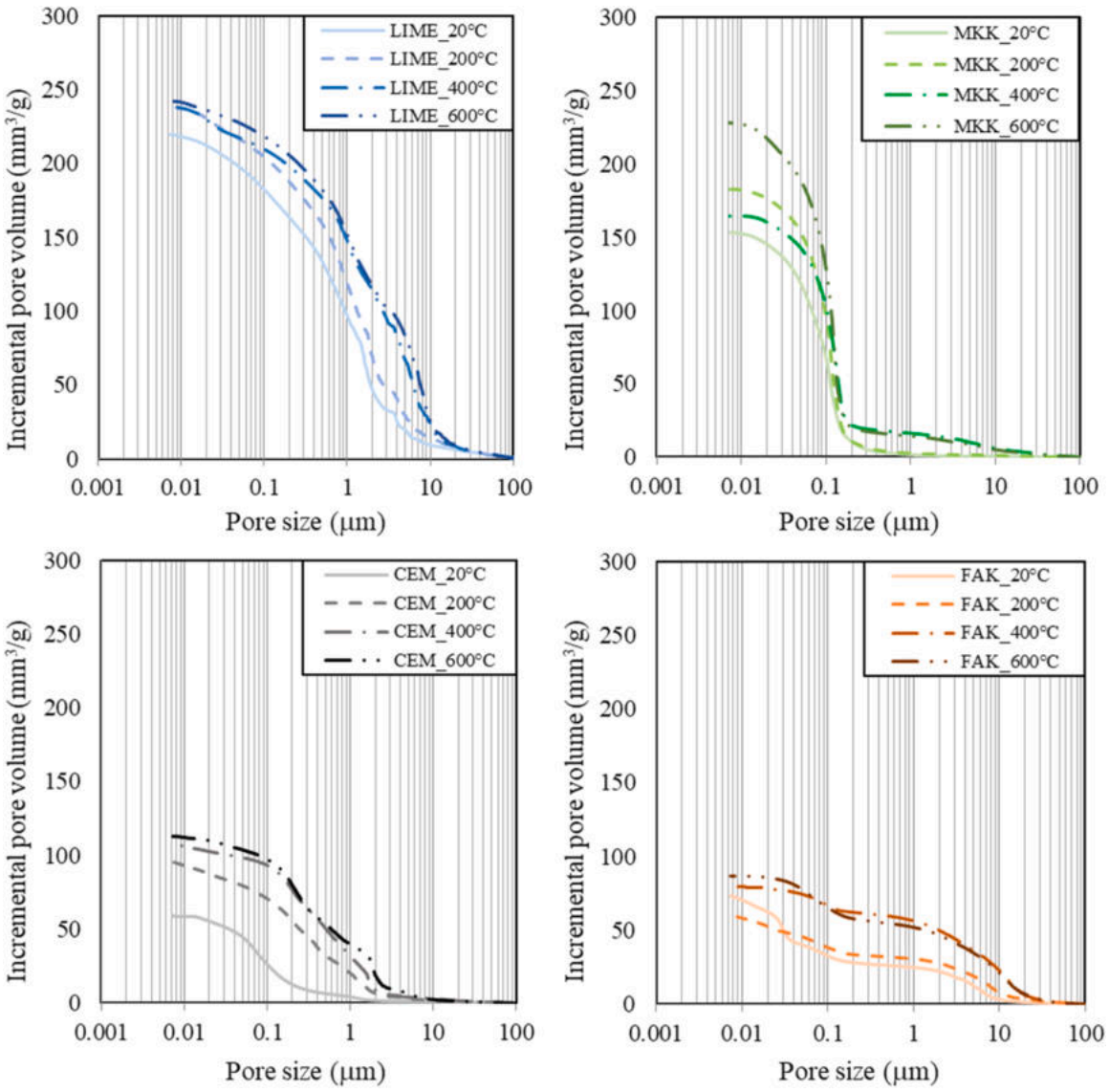


Fig. 15. Pore size distribution of mortars after exposure to 20 °C, 200 °C, 400 °C, and 600 °C.

showed an increase of about 24%. These trends are in line with those observed for the flexural strength of the corresponding matrices after thermal exposure. As evidenced by SEM observations (Fig. 11), exposure to 200 °C does not appear to significantly degrade the polymeric coating of the basalt yarns, which melts and subsequently re-solidifies during cooling, without markedly affecting the overall mechanical performance of the TRM composite. The modulus of elasticity in the cracked phase generally decreases as the exposure temperature increases, except for the MKK system, which shows an increase after exposure to 200 °C. In contrast, when the exposure temperature increased to 400 °C, all TRM systems exhibited a pronounced reduction in tensile strength. This reduction is particularly severe for the lime-based system (−77%), while it is more moderate for the FAK (−27%) and CEM (−33%) systems. In general, the modulus of elasticity in the cracked phase ($E_{2,TRM}$) and the strain at the maximum load ($\varepsilon_{max,TRM}$) decrease significantly after exposure to 400 °C, due to the degradation of the polymeric coating, which leads to a marked bond reduction at the textile-to-matrix interface. CEM systems are the only ones that retain a certain level of tensile strength and stiffness after exposure to 400 °C. At an exposure temperature of 600 °C, the degradation became critical for all TRM systems, with tensile strength reductions exceeding 70%, indicating a substantial loss of structural effectiveness.

In all cases, the observed failure mode is governed by textile slippage within the mortar matrix, accompanied by the formation and propagation of multiple cracks (Figs. 20 and 21). Fig. 20 shows that the LIME and MKK specimens exhibit more widespread cracking than the FAK and CEM matrix systems, likely due to the lower mechanical resistance of the former two matrices. Furthermore, it is observed that as the temperature increases, the damage is concentrated in a smaller number of cracks, one of which propagates until failure.

Finally, Fig. 22 presents comparative graphs illustrating the evolution of the mechanical properties of basalt yarn and TRM composites as a function of temperature. As previously highlighted, after exposure to 200 °C, the mechanical properties of the basalt yarn remain largely unaffected, whereas those of the TRM systems exhibit variations of up to approximately 20%. In particular, the TRM-MKK systems show an increase in tensile strength and cracked modulus of elasticity, which can be attributed to the enhancement of the matrix mechanical properties (as explained in Section 3.6). Conversely, the tensile strength of TRM systems decreases by approximately 10% and 20% in the CEM- and FAK-based matrices, respectively. This reduction is likely associated with the decrease in flexural strength of the CEM and FAK matrices after exposure to 200 °C, probably due to the formation of microcracks within the matrix.

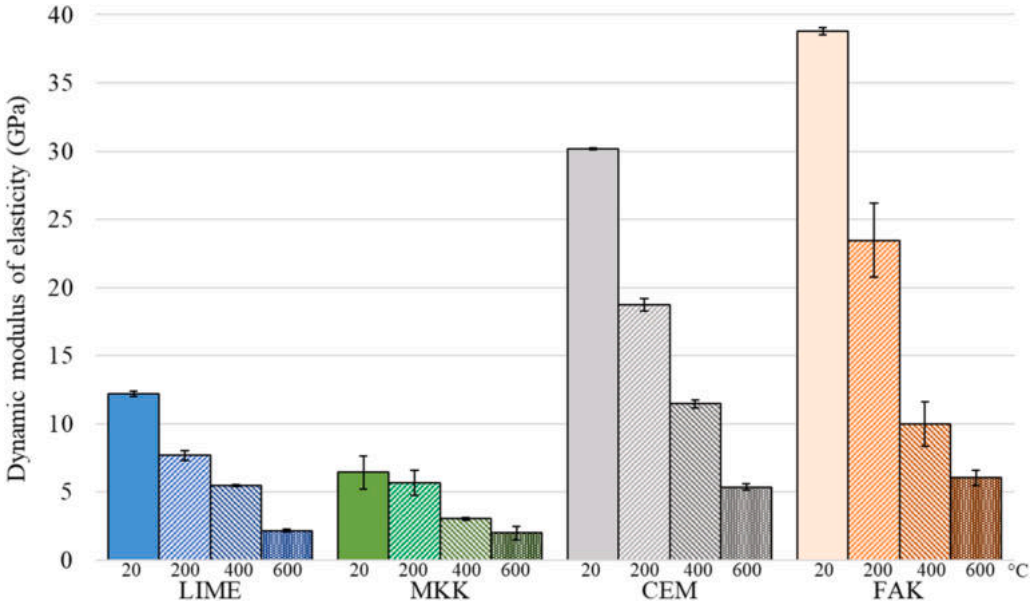


Fig. 16. Dynamic modulus of elasticity of mortars after exposure to 20 °C, 200 °C, 400 °C, and 600 °C.

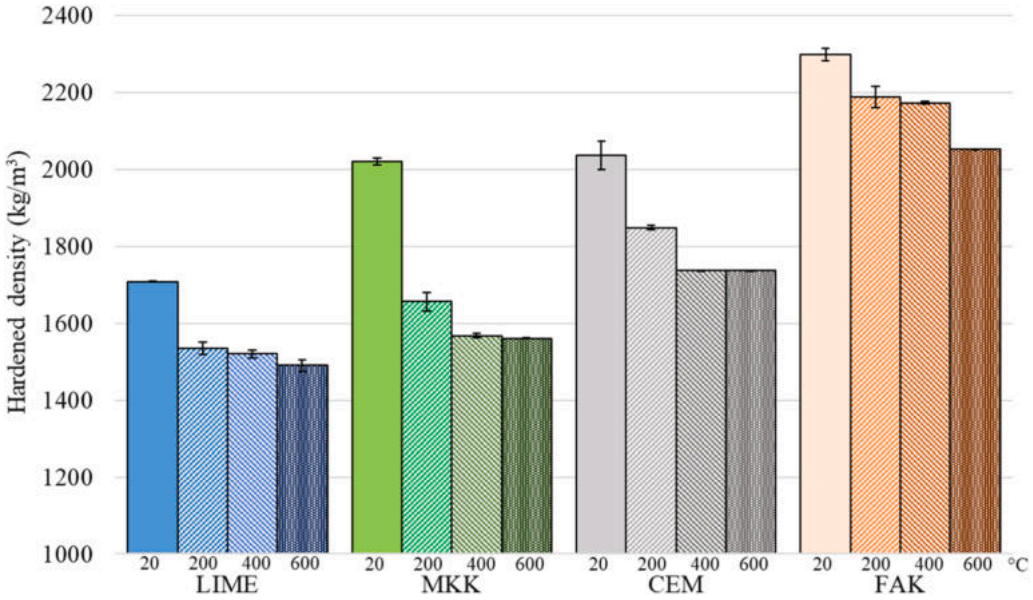


Fig. 17. Hardened density of mortars after exposure to 20 °C, 200 °C, 400 °C, and 600 °C.

Table 5
Results of tensile tests on basalt yarns after temperature exposure, COV in round brackets.

Temp. (°C)	σ_{yarn} (MPa)	$\varepsilon_{yarn,max}$ (mm/mm)	E_{yarn} (GPa)	Variation of σ_{yarn}
20	1346 (10%)	0.0225 (3%)	79 (4%)	-
200	1306 (5%)	0.0203 (11%)	77 (5%)	-3%
400	278 (23%)	0.0090 (22%)	36 (14%)	-79%
600	44 (21%)	-	-	-97%

When the exposure temperature increases to 400 °C, the tensile strength of the basalt yarn decreases drastically, by approximately 80%. This severe degradation leads to a pronounced reduction in the tensile strength of the corresponding TRM systems. Nevertheless, the presence of the inorganic matrix partially mitigates this loss by exerting a protective effect, thereby reducing the extent of thermal degradation of the basalt textile. In contrast, such protective capacity is practically absent in lime-based matrices, which are unable to effectively limit the strength degradation of the textile reinforcement.

3.9. Critical comparison with existing literature

Although experimental investigations on TRM systems subjected to elevated temperatures are still relatively limited, it is still valuable to provide a brief comparison with the available literature. Direct comparison is, however, hindered by the absence of a standardized testing protocol for assessing the residual mechanical performance of TRM systems after thermal exposure. Differences in experimental methodologies, such as temperature ranges, heating durations, and gripping configurations adopted in tensile tests, further complicate meaningful comparisons.

Table 6
Results of tensile tests on TRM coupons, COV in round brackets.

Specimen	$\sigma_{1,TRM}$ (MPa)	$\sigma_{max,TRM}$ (MPa)	$\varepsilon_{max,TRM}$	$E_{2,TRM}$ (GPa)	Expl. ratio (%)	Loss/gain of tensile strength
T_LIME_20	191 (46%)	420 (1%)	0.0124 (18%)	41 (5%)	31.2	-
T_LIME_200	184 (11%)	401 (16%)	0.0083 (27%)	42 (37%)	29.8	-5%
T_LIME_400	-	98 (17%)	0.0393 (22%)	-	7.3	-77%
T_LIME_600	-	74 (29%)	0.0393 (55%)	-	5.5	-82%
T_MKK_20	273 (-)	388 (4%)	0.0090 (32%)	15 (28%)	28.8	-
T_MKK_200	304 (37%)	481 (19%)	0.0152 (37%)	21 (28%)	35.7	+ 24%
T_MKK_400	-	212 (10%)	0.0131 (30%)	7 (46%)	15.6	-45%
T_MKK_600	-	117 (32%)	0.0435 (82%)	-	8.7	-70%
T_CEM_20	467 (38%)	604 (13%)	0.0151 (82%)	49 (20%)	44.9	-
T_CEM_200	379 (18%)	545 (9%)	0.0094 (19%)	37 (60%)	40.5	-10%
T_CEM_400	-	405 (7%)	0.0133 (10%)	34 (46%)	30.1	-33%
T_CEM_600	-	136 (16%)	0.0443 (65%)	-	10.0	-77%
T_FAK_20	252 (7%)	400 (3%)	0.0244 (40%)	31 (8%)	29.7	-
T_FAK_200	161 (-)	324 (1%)	0.0175 (61%)	27 (18%)	24.0	-19%
T_FAK_400	-	294 (13%)	0.0185 (105%)	15 (42%)	21.8	-27%
T_FAK_600	-	93 (50%)	0.0301 (121%)	-	6.9	-77%

The literature studies most comparable to the present work, particularly in terms of maximum exposure temperatures, are summarized in Table 7. The table lists the matrix and reinforcement materials, exposure durations, and the types of grips used in tensile testing. For consistency, the ultimate residual tensile strength of the TRM systems after exposure to temperatures up to 600 °C was selected as the comparison parameter. To facilitate comparison across studies, tensile strengths were normalized with respect to their corresponding room-temperature values (Fig. 23). Moreover, to enhance the relevance of the comparison and account for similarities in mortar mechanical properties, TRM systems with lime-based matrices were compared with those incorporating alkali-activated metakaolin-based matrices, while systems with cementitious matrices were compared with alkali-activated fly ash-based systems.

Fig. 23a compares the normalized residual tensile strength of TRM systems with lime- and metakaolin-based matrices from the present study (LIME and MKK) with comparable systems reported by Estevan et al. [31]. A consistent trend is observed for all lime-based systems: modest strength retention or a slight increase up to 100–200 °C, followed by a sharp degradation beyond 400 °C. When focusing on lime-based matrices reinforced with basalt mesh, Estevan's results closely match those of the present study, particularly at 400 °C and 600 °C. The strength increase at intermediate temperatures (100–200 °C), especially noticeable for some literature systems and the MKK system, can be attributed to continued matrix hydration and densification, as well as re-solidification of the polymeric coating, which enhances adhesion with the inorganic matrix. This effect is particularly pronounced in TRM systems with coated fabrics. At 400 °C, however, all systems undergo pronounced strength loss due to coating decomposition, textile-matrix debonding, and extensive matrix microcracking. Notably, the metakaolin-based TRM exhibits higher residual strength at both 400 °C and 600 °C compared to lime-based systems, indicating superior thermal stability and more effective preservation of composite properties.

Fig. 23b presents a similar comparison for cement-based and alkali-activated (fly ash-based) TRM systems. Despite some scatter due to differences in testing protocols, textile types, and exposure durations, a consistent degradation pattern emerges. Most systems show either stable or slightly improved tensile performance up to 100–200 °C, followed by progressive strength loss at higher temperatures. The results of the present study (CEM and FAK) align well with those reported in the literature, particularly up to 400 °C. At this temperature, cementitious and alkali-activated matrices retain a higher fraction of their original tensile capacity compared to lime-based systems, suggesting a greater ability to limit thermal damage to the basalt textile. At 600 °C, however, all systems converge toward very low residual strengths, reflecting severe degradation of both the reinforcement and the matrix, and near-complete loss of load-transfer capability.

Focusing specifically on basalt-reinforced systems, Yang et al. [63] reported a residual tensile strength retention of approximately 67% at 300 °C. In comparison, the CEM system investigated in the present study demonstrates superior thermal performance, maintaining a comparable retention level (67%) even at the higher temperature of 400 °C.

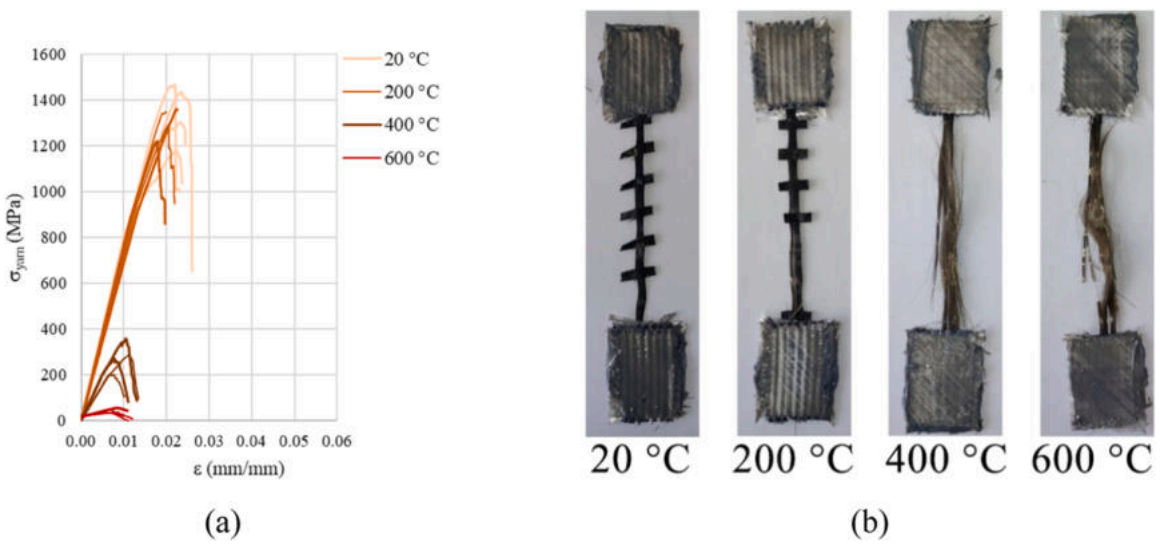


Fig. 18. (a) Stress-strain curves and (b) failure modes of basalt yarns after exposure to 20 °C, 200 °C, 400 °C, and 600 °C.

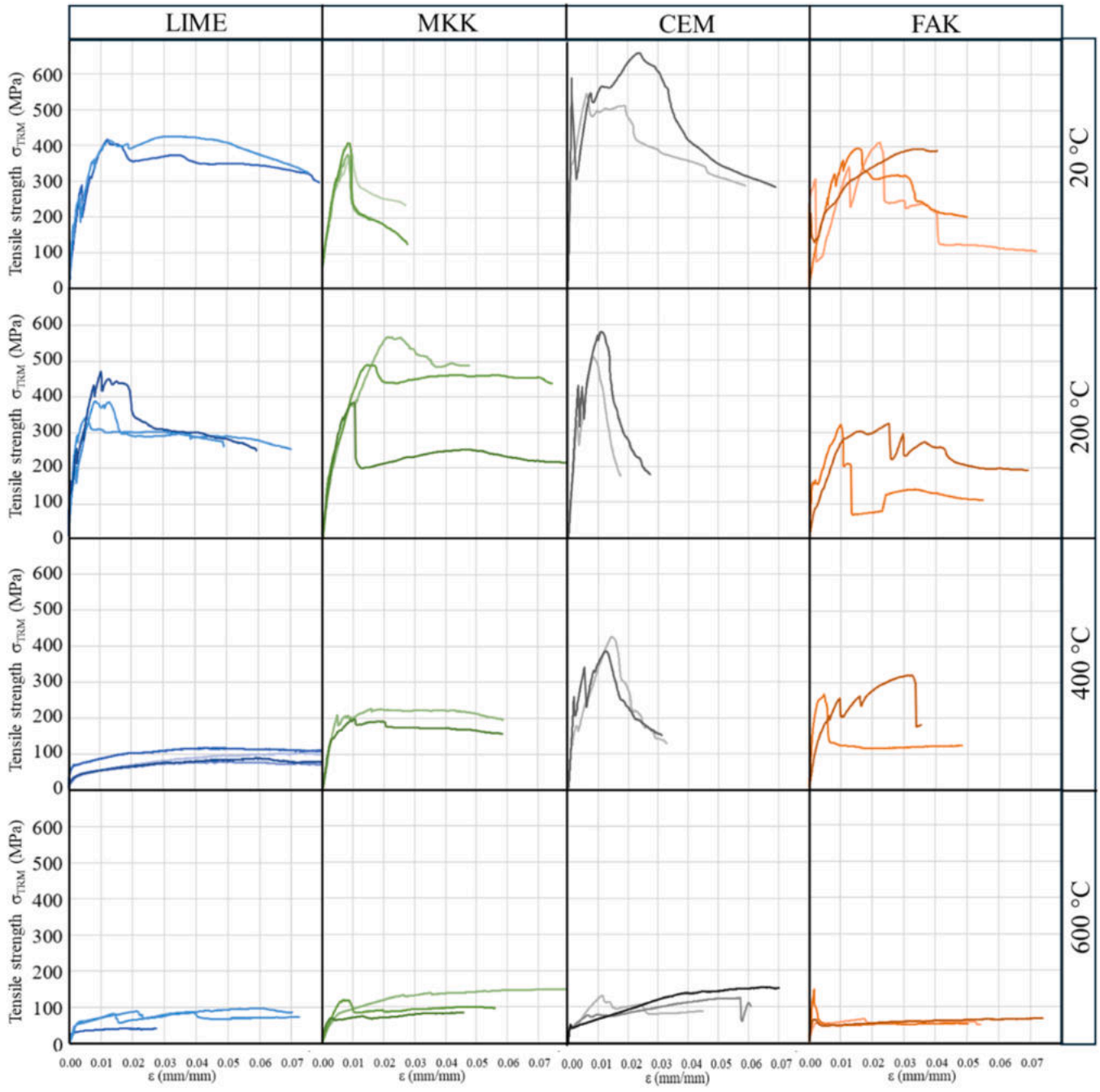


Fig. 19. Stress-strain curves of TRM coupons after exposure to 20, 200, 400 and 600 °C.

Although Milling et al. [65] employed high-strength alkali-resistant basalt fibers, their systems exhibited a catastrophic strength reduction at 400 °C, retaining only 10% of the original capacity (160 MPa). In contrast, the CEM and FAK series in the present study preserved substantially higher residual tensile strengths (405 MPa and 294 MPa, respectively), thereby highlighting their enhanced thermal protection capacity and improved resistance to high-temperature degradation.

Overall, despite the inherent variability among studies, the comparison highlights consistent temperature-dependent trends and confirms that matrix composition plays a key role in governing the residual tensile performance of TRM systems after high-temperature exposure.

4. Conclusions

The present study aimed at investigating the residual performances of TRM systems incorporating alkali-activated mortars in comparison with conventional lime- and cement-based matrices, reinforced with coated basalt textile, and exposed to elevated temperatures up to 600 °C.

Based on the experimental results, the following conclusions can be drawn:

- At room temperature, TRM systems incorporating alkaline-activated matrices (TRAAMs) generally exhibit lower mechanical properties compared to those with lime- or cement-based matrices. This behavior is likely attributed to the limited compatibility and lower adhesion between alkaline-activated matrices and the polyester-based polymer coating of the basalt textile used in this study.
- Exposure to temperatures up to 200 °C had a negligible or even beneficial effect on the mechanical performance of the investigated TRM systems. In particular, both TRAAM systems exhibited

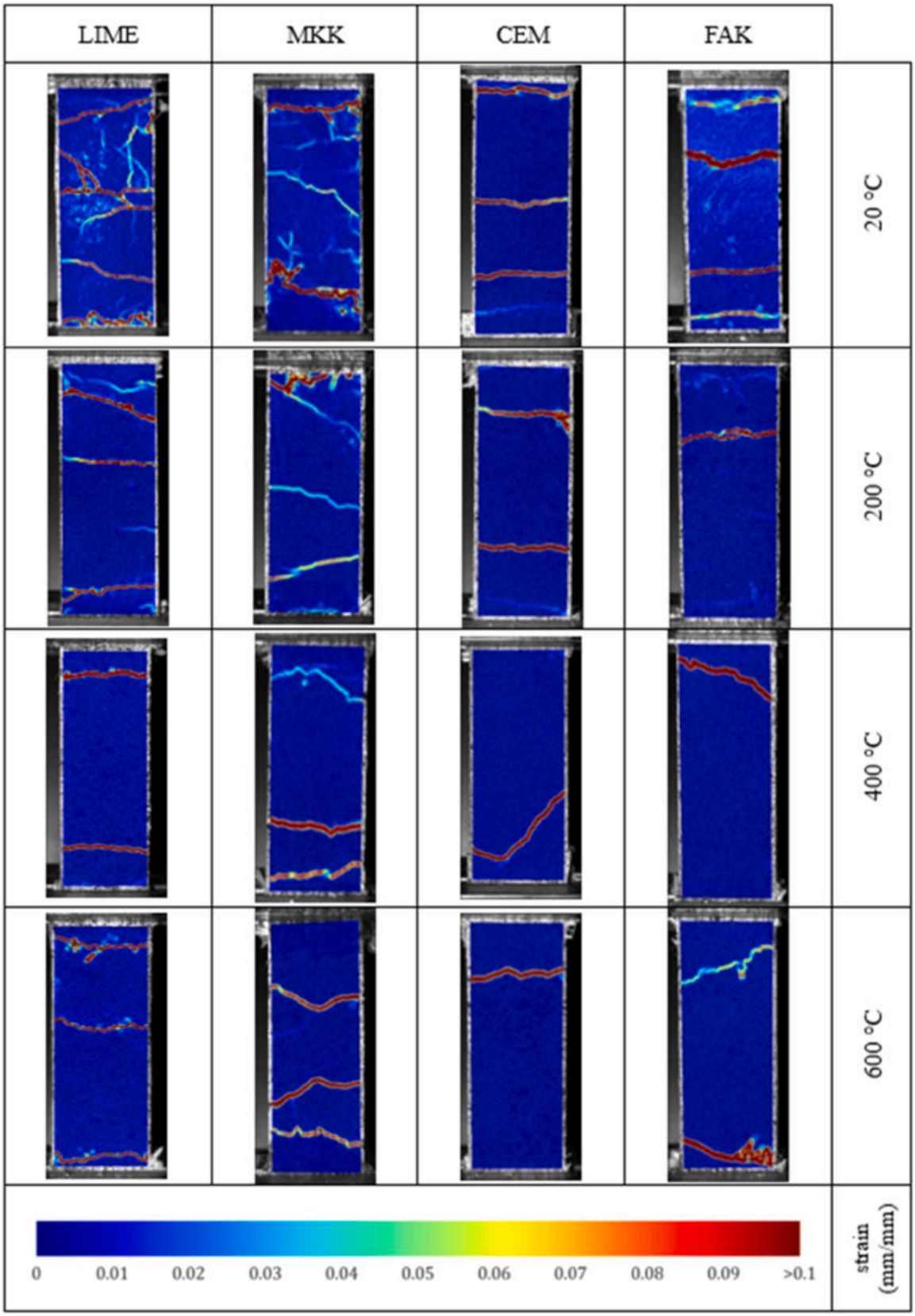


Fig. 20. Strain distribution and crack pattern of TRM coupons after exposure to 20 °C, 200 °C, 400 °C, and 600 °C.

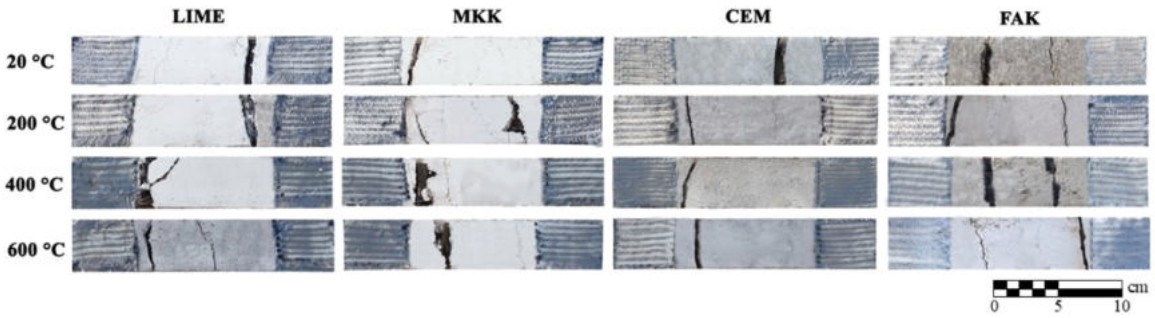


Fig. 21. Failure modes of TRM coupons after exposure to 20 °C, 200 °C, 400 °C, and 600 °C.

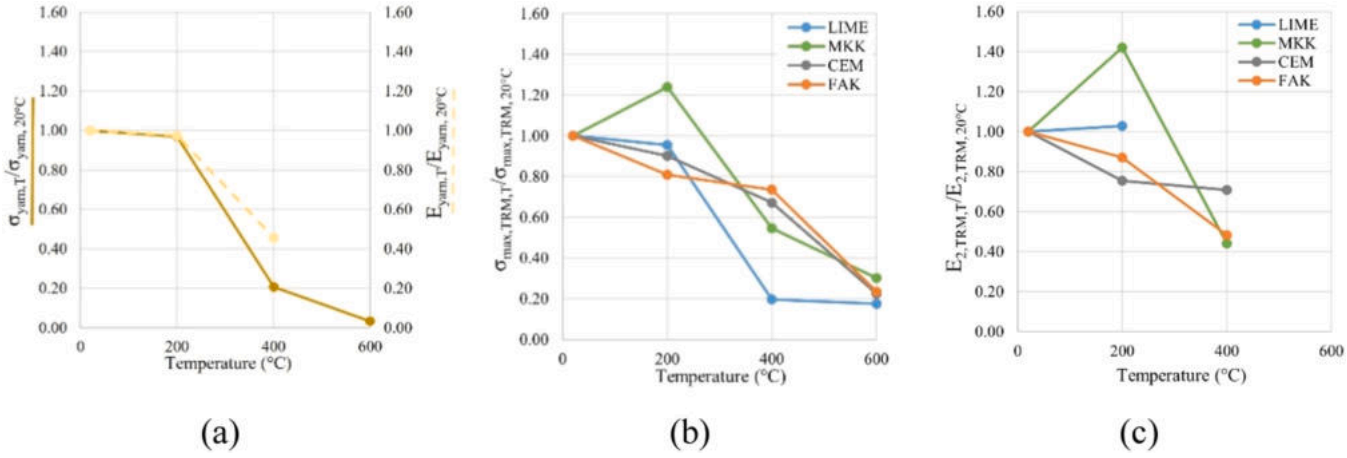


Fig. 22. Comparative analysis of the main properties of (a) basalt yarn and (b,c) TRM composites after exposure to 20 °C, 200 °C, 400 °C, and 600 °C.

Table 7
Studies from the literature.

Authors	Mortar matrix	Textile (coating)	Temperature (°C)	Exp. time (h)	Grip type
Estevan et al. [31]	Hydraulic Lime 1	Glass 1 (thermosetting resin)	20–100–200–400–600	1	Clevis
	Hydraulic Lime 2	Glass 2 (unspecified polymer)	20–100–200–400–600	1	Clevis
	Hydraulic Lime 2	Carbon (uncoated)	20–100–200–400–600	1	Clevis
	Hydraulic Lime 2	Basalt (unspecified polymer)	20–100–200–400–600	1	Clevis
De Andrade Silva et al. [32]	Cementitious	Carbon (uncoated)	20–100–150–200–400–600	2	Clamp
	Cementitious	Carbon (unspecified polymer)	20–100–150–200–400–600	2	Clamp
Yang et al. [63]	Cementitious	Basalt (high temperature resistive coating)	20–100–200–300	8	Clevis
	Cementitious	Carbon (high temperature resistive coating)	20–100–200–300	8	Clevis
	Cementitious	Glass (SBR coated)	20–100–200–300	8	Clevis
Kapsalis et al. [64]	Cementitious	Carbon (uncoated)	20–200–400–600	1	Clevis
	Ferronickel slag (AAM)	Carbon (uncoated)	20–200–400–600	1	Clevis
Milling et al. [65]	Cementitious	Basalt (unspecified polymer)	20–100–200–300–400	1	Clamp

slight increases in compressive and tensile strengths, attributed to dehydration-induced densification and further polymerization of the aluminosilicate network. At this temperature, the polyester coating of the basalt textile melted and re-solidified upon cooling without significant loss of fiber integrity or textile-matrix bond.

- The residual mechanical performance of TRM systems is strongly influenced by the type of inorganic matrix. Metakaolin-based AAMs showed superior thermal stability among the low-strength matrices, retaining most of their compressive strength even after exposure to 600 °C, whereas lime-based mortars experienced marked degradation beyond 400 °C due to portlandite decomposition and microcracking. CEM and FAK mortars displayed comparable strength levels at room temperature and similar degradation trends at higher temperatures, although fly ash-based AAMs benefited from strength enhancement at 200 °C.
- A pronounced reduction in both mortar and TRM tensile performance occurred after exposure to 400 °C, becoming critical at 600 °C. This degradation is primarily attributed to irreversible matrix dehydration (portlandite decomposition in lime and water vapor release in LIME and CEM), increased total porosity, microcracking, and, most critically, the decomposition of the polyester coating on the basalt textile. SEM observations and yarn tensile tests confirmed that the loss of coating integrity caused filament debonding and severe reductions in fiber tensile capacity.
- At 400 °C, TRM systems retained higher tensile capacity than isolated basalt yarns exposed to the same temperature, indicating a partial protective effect of the mortar matrix. This effect was more pronounced for CEM and FAK matrices, which better preserved composite performance and limited thermal damage to the textile compared to lime-based systems.

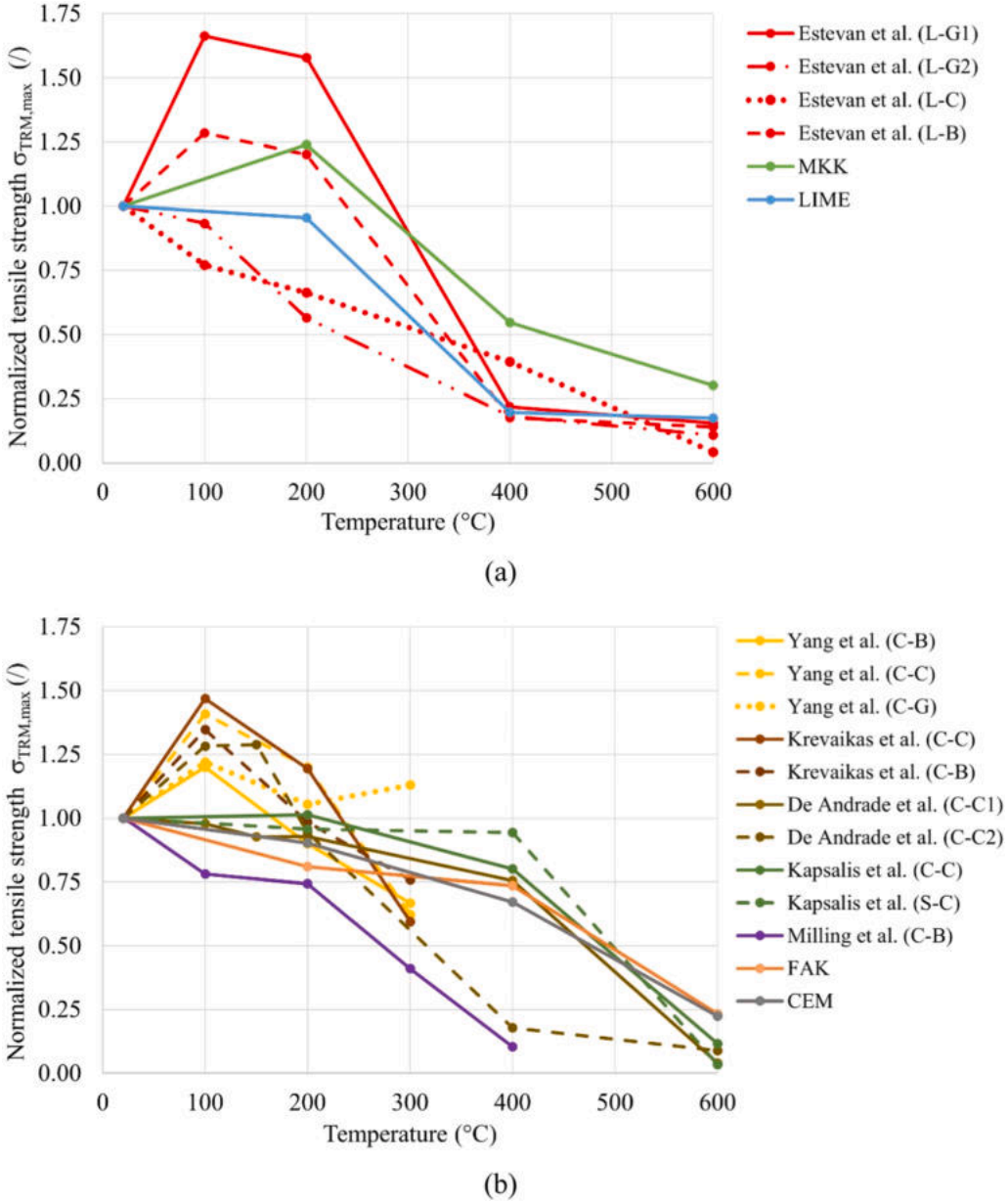


Fig. 23. Comparison of normalized residual tensile strength of TRM systems after high temperature exposure: (a) low-strength mortar matrices and (b) medium-strength mortar matrices.

- Comparison with literature data confirmed consistent temperature-dependent trends across different TRM systems, despite variations in materials and testing protocols. Most systems exhibited stable or slightly improved performance up to 200 °C, followed by a sharp drop beyond 400 °C. These findings further emphasize the critical role of matrix composition in governing the residual tensile strength of TRM composites under high-temperature exposure.

In summary, the TRAAM systems investigated in the present study did not demonstrate a significant improvement in the mechanical performance of TRM composites compared to those incorporating conventional matrices after high temperatures exposure. Although some enhancement in properties was observed at 200 °C, exposure to higher temperatures (from 400 °C onward) resulted in severe degradation across all TRM systems. The pronounced deterioration observed at temperatures $\geq$ 400 °C underscores the need for further developments, particularly in high-temperature-resistant textile coatings and thermally stable matrices, to expand the applicability of TRM systems in fire-exposed or high-temperature environments.

CRediT authorship contribution statement

Jacopo Donnini: Writing – original draft, Supervision, Resources, Investigation, Data curation, Conceptualization. **Valeria Corinaldesi:** Supervision, Resources, Conceptualization. **Gianluca Chiappini:** Writing – review & editing, Validation, Software, Methodology, Investigation, Formal analysis, Data curation, Conceptualization. **Mobili Alessandra:** Writing – original draft, Validation, Methodology, Investigation, Data curation, Conceptualization. **Daniele Berdini:** Writing – original draft, Software, Investigation, Formal analysis, Data curation.

Declaration of Competing Interest

The authors declare that they have no known competing financial interests or personal relationships that could have appeared to influence

the work reported in this paper.

Data availability

Data will be made available on request.

References

[1] A. Nanni, A new tool for concrete and masonry repair, Concr. Int. 34 (2016) 43–49.
[2] C.G. Papanicolaou, T.C. Triantafillou, K. Karlos, M. Papathanasiou, Textile-reinforced mortar (TRM) versus FRP as strengthening material of URM walls: in-plane cyclic loading, Mater. Struct. 40 (2006) 1081–1097, https://doi.org/10.1617/s11527-006-9207-8.
[3] L.N. Koutas, Z. Tetta, D.A. Bournas, T.C. Triantafillou, Strengthening of concrete structures with textile reinforced mortars: state-of-the-art review, J. Compos. Constr. 23 (2019) 03118001, https://doi.org/10.1061/(ASCE)CC.1943-5614.0000882.
[4] G. De Felice, S. De Santis, L. Garmendia, B. Ghiassi, P. Larrinaga, P.B. Lourenço, et al., Mortar-based systems for externally bonded strengthening of masonry, Materia (2021) 2021–2037, https://doi.org/10.1617/s11527-014-0360-1.
[5] Y. Yardim, O. Lalaj, Shear strengthening of unreinforced masonry wall with different fiber reinforced mortar jacketing, Constr. Build. Mater. 102 (2016) 149–154, https://doi.org/10.1016/j.conbuildmat.2015.10.095.
[6] T. D'Antino, F.G. Carozzi, C. Poggi, Diagonal shear behavior of historic walls strengthened with composite reinforced mortar (CRM, Mater. Struct. 52 (2019) 1–15, https://doi.org/10.1617/s11527-019-1414-1.
[7] A. Bilotta, F. Ceroni, E. Nigro, M. Pecce, Experimental tests on FRCM strengthening systems for tuff masonry elements, Constr. Build. Mater. 138 (2017) 114–133, https://doi.org/10.1016/j.conbuildmat.2017.01.124.
[8] J. Donnini, G. Maracchini, S. Lenci, V. Corinaldesi, E. Quagliarini, TRM reinforced tuff and fired clay brick masonry: experimental and analytical investigation on their in-plane and out-of-plane behavior, Constr. Build. Mater. 272 (2021) 121643, https://doi.org/10.1016/j.conbuildmat.2020.121643.
[9] L.N. Koutas, Z. Tetta, D.A. Bournas, T.C. Triantafillou, Strengthening of concrete structures with textile reinforced mortars: State-of-the-art review, J. Compos. Constr. 23 (2019) 03118001, https://doi.org/10.1061/(ASCE)CC.1943-5614.0000882.
[10] O. Awani, T. El-Maaddawy, N. Ismail, Fabric-reinforced cementitious matrix: a promising strengthening technique for concrete structures, Constr. Build. Mater. 132 (2017) 94–111, https://doi.org/10.1016/j.conbuildmat.2016.11.125.
[11] L.N. Koutas, C.G. Papakonstantinou, Flexural strengthening of RC beams with textile-reinforced mortar composites focusing on the influence of the mortar type, Eng. Struct. 246 (2021) 113060, https://doi.org/10.1016/j.engstruct.2021.113060.
[12] T. El-Maaddawy, A. El Refai, Innovative repair of severely corroded t-beams using fabric-reinforced cementitious matrix, J. Compos. Constr. 20 (2016) 04015073, https://doi.org/10.1061/(ASCE)CC.1943-5614.000064.
[13] R.K. Majhi, S.-C. Shin, J.M. Kim, S.K. Patro, Towards Sustainable Cement: Review of Blended Binder Systems and Performance-Based Specification Strategies, Mater. Today Sustain (2026) 101328, https://doi.org/10.1016/j.mtsust.2026.101328.
[14] S.A. Ishak, H. Hashim, Low carbon measures for cement plant - a review, J. Clean. Prod. 103 (2015) 260–274, https://doi.org/10.1016/j.jclepro.2014.11.003.
[15] J. Donnini, A. Mobili, G. Maracchini, G. Chiappini, F. Tittarelli, V. Corinaldesi, A multi-performance comparison between lime, cementitious and alkali-activated TRM systems: mechanical, environmental and energy perspectives, Constr. Build. Mater. 440 (2024) 137396, https://doi.org/10.1016/j.conbuildmat.2024.137396.
[16] J.L. Provis, Geopolymers and other alkali activated materials: why, how, and what, Mater. Struct. 47 (2013) 11–25, https://doi.org/10.1617/s11527-013-0211-5.
[17] X. Wang, F. Li, F. Gao, Y. Wang, M. Li, J. Wang, et al., Characteristics of alkali-activated slag mortar under combined freeze-thaw cycles and sulfate exposure: microstructural and mechanical insights, Constr. Build. Mater. 493 (2025) 143087, https://doi.org/10.1016/j.conbuildmat.2025.143087.
[18] C. Giosuè, A. Mobili, C. Di Perna, F. Tittarelli, Performance of lightweight cement-based and alkali-activated mortars exposed to high-temperature, Constr. Build. Mater. 220 (2019) 565–576, https://doi.org/10.1016/j.conbuildmat.2019.05.193.
[19] T. Wu, S. Tang, Y.-R. Dong, J.-H. Luo, A review of the thermal and mechanical characteristics of alkali-activated composites at elevated temperatures, Buildings 15 (2025) 738, https://doi.org/10.3390/buildings15050738.
[20] P.D. Askouni, P. Kapsalis, C.G. Papanicolaou, T.C. Triantafillou, Strengthening of masonry and concrete members with textile-reinforced alkali-activated mortars: a review on the mechanical performance, Materials 18 (2025) 1517, https://doi.org/10.3390/ma18071517.
[21] F.A. Obaida, T. El-Maaddawy, H. El-Hassan, Bond behavior of carbon fabric-reinforced matrix composites: geopolymeric matrix versus cementitious mortar, Buildings 11 (2021) 207, https://doi.org/10.3390/buildings11050207.
[22] P. Kapsalis, P.D. Askouni, C.G. Papanicolaou, T.C. Triantafillou, Cementitious versus alkali-activated textile-reinforced mortars combined with mineral wool insulation for strengthening masonry panels exposed to high temperature, Constr. Build. Mater. 474 (2025) 141133, https://doi.org/10.1016/j.conbuildmat.2025.141133.
[23] Bisby L., Stratford T., Hart C., Farren S. Fire performance of well-anchored TRM, FRCM and FRP flexural strengthening systems. In: Whysall CJ, Taylor SE, editors. Adv. Compos. Constr. Netw. Gr. Compos. Constr., Chesterfield, UK: 2013, p. 113.
[24] J. Michels, D. Zwicky, J. Scherer, Y.E. Harmanci, M. Motavalli, Structural strengthening of concrete with fiber reinforced cementitious matrix (frcm) at ambient and elevated temperature – recent investigations in Switzerland, Adv. Struct. Eng. 17 (2014) 1785–1800, https://doi.org/10.1260/1369-4332.17.12.1785.
[25] P. Mazzuca, A. Micieli, F. Campolongo, L. Ombres, Influence of thermal exposure scenarios on the residual mechanical properties of a cement-based composite system, Constr. Build. Mater. 466 (2025) 140304, https://doi.org/10.1016/j.conbuildmat.2025.140304.
[26] Z.C. Tetta, D.A. Bournas, TRM vs FRP jacketing in shear strengthening of concrete members subjected to high temperatures, Compos Part B Eng. 106 (2016) 190–205, https://doi.org/10.1016/j.compositesb.2016.09.026.
[27] S.R. Maroudas, C.C.G. Papanicolaou, Effect of high temperatures on the TRM-to-Masonry bond, Key Eng. Mater. 747 (2017) 533–541, https://doi.org/10.4028/www.scientific.net/KEM.747.533.
[28] P.D. Askouni, C.C.G. Papanicolaou, M.I. Kaffetzakis, The effect of elevated temperatures on the TRM-to-masonry bond: comparison of normal weight and lightweight matrices, Appl. Sci. 9 (2019) 2156, https://doi.org/10.3390/app9102156.
[29] P.D. Askouni, C.C.G. Papanicolaou, L. Azdejkovic, Experimental investigation of the TRM-to-masonry bond after exposure to elevated temperatures: cementitious and alkali-activated matrices of various densities, Materials 15 (2022) 140, https://doi.org/10.3390/ma15010140.
[30] L. Estevan, F.J. Baeza, F.B. Varona, J. Pereiro, Effect of high temperature on textile reinforced Mortar-to-masonry bond, Constr. Build. Mater. 393 (2023) 132123, https://doi.org/10.1016/j.conbuildmat.2023.132123.
[31] L. Estevan, F.B. Varona, F.J. Baeza, B. Torres, D. Bru, Textile Reinforced Mortars (TRM) tensile behavior after high temperature exposure, Constr. Build. Mater. 328 (2022) 127116, https://doi.org/10.1016/j.conbuildmat.2022.127116.
[32] F. de Andrade Silva, M. Butler, S. Hempel, R. Dias Toledo Filho, V. Mechtcherine, Effects of elevated temperatures on the interface properties of carbon textile-reinforced concrete, Cem. Concr. Compos. 48 (2014) 26–34, https://doi.org/10.1016/j.cemconcomp.2014.01.007.
[33] V. Fiore, T. Scalici, G.Di Bella, A. Valenza, A review on basalt fibre and its composites, Compos. Part B Eng. 74 (2015) 74–94, https://doi.org/10.1016/j.compositesb.2014.12.034.
[34] F. Roscini, F. Nerilli, B. Ferracuti, M. Guadagnini, Experimental and numerical investigation of the bond interface between basalt fibre and mortar in TRM system, Constr. Build. Mater. 487 (2025) 142064.
[35] C. Wan, J. Wang, L. Shen, F. Yang, Q. Zeng, L. Ye, Confinement mechanism and modeling of basalt TRM confined concrete: effect of mortar matrix grade, Eng. Struct. 312 (2024) 118227, https://doi.org/10.1016/j.engstruct.2024.118227.
[36] T. Li, Y. Zhang, J.-G. Dai, Flexural behavior and microstructure of hybrid basalt textile and steel fiber reinforced alkali-activated slag panels exposed to elevated temperatures, Constr. Build. Mater. 152 (2017) 651–660, https://doi.org/10.1016/j.conbuildmat.2017.07.059.
[37] S. Tamburini, M. Natali, E. Garbin, M. Panizza, M. Favaro, M.R. Valluzzi, Geopolymer matrix for fibre reinforced composites aimed at strengthening masonry structures, Constr. Build. Mater. 141 (2017) 542–552, https://doi.org/10.1016/j.conbuildmat.2017.03.017.
[38] EN 1097-6:2022 - Tests for mechanical and physical properties of aggregates - Part 6: Determination of particle density and water absorption 2022.
[39] A. Mobili, A. Belli, C. Giosuè, T. Bellezze, F. Tittarelli, Metakaolin and fly ash alkali-activated mortars compared with cementitious mortars at the same strength class, Cem. Concr. Res. 88 (2016) 198–210, https://doi.org/10.1016/j.cemconres.2016.07.004.
[40] EN 1504-3:2006 - Products and systems for the protection and repair of concrete structures - Definitions, requirements, quality control and evaluation of conformity - Part 3: Structural and non-structural repair 2006.
[41] EN 1015-3:2007 - Methods of test for mortar for masonry - Part 3: Determination of consistence of fresh mortar (by flow table) 2007.
[42] EN 1015-11:1999/A1:2006 - Methods of test for mortar for masonry - Part 11: Determination of flexural and compressive strength of hardened mortar 2006.
[43] EN 12504-4:2004 - Testing concrete in structures - Part 4: Determination of ultrasonic pulse velocity 2004.
[44] Linea Guida per la identificazione, la qualificazione ed il controllo di accettazione di compositi fibrorinforzati a matrice inorganica (FRCM) da utilizzarsi per il consolidamento strutturale di costruzioni esistenti. Consiglio Superiore dei Lavori Pubblici; 2022.
[45] EN 2561:1995 - Aerospace series - Carbon fibre reinforced plastics - Unidirectional laminates - Tensile test parallel to the fibre direction 1995.
[46] J. Donnini, F. De Caso y Basalo, V. Corinaldesi, G. Lancioni, A. Nanni, Fabric-reinforced cementitious matrix behavior at high-temperature: experimental and numerical results, Compos Part B 108 (2017) 108–121, https://doi.org/10.1016/j.compositesb.2016.10.004.
[47] M.U. Yılmazoğlu, İ. Türkel, A. Benli, O.Y. Bayraktar, M. Bilgehan, G. Kaplan, Sustainable enhancement of alkali-activated foam concrete using vegetable waste ash and fly ash: improving mechanical, thermal, and durability properties, J. Build. Eng. 110 (2025) 113091, https://doi.org/10.1016/j.jobe.2025.113091.
[48] F. Pacheco-Torgal, D. Moura, Y. Ding, S. Jalali, Composition, strength and workability of alkali-activated metakaolin based mortars, Constr. Build. Mater. 25 (2011) 3732–3745, https://doi.org/10.1016/j.conbuildmat.2011.04.017.
[49] D.A.S. Rambo, F. De Andrade Silva, R.D. Toledo Filho, O. Gomes, Effect of elevated temperatures on the mechanical behavior of basalt textile reinforced refractory concrete, Mater. Des. 65 (2015) 24–33, https://doi.org/10.1016/j.matdes.2014.08.060.

[50] A. Behnood, M. Ghandehari, Comparison of compressive and splitting tensile strength of high-strength concrete with and without polypropylene fibers heated to high temperatures, Fire Saf. J. 44 (2009) 1015–1022, https://doi.org/10.1016/j.firesaf.2009.07.001.
[51] C. Rodriguez-Navarro, K. Kudlacz, A. Ruiz-Agudo, The mechanism of thermal decomposition of dolomite: New insights from 2D-XRD and TEM analyses, Am. Miner. 97 (2012) 38–51, https://doi.org/10.2138/am.2011.3813.
[52] H.Y. Zhang, V. Kodur, S.L. Qi, L. Cao, B. Wu, Development of metakaolin-fly ash based geopolymers for fire resistance applications, Constr. Build. Mater. 55 (2014) 38–45, https://doi.org/10.1016/j.conbuildmat.2014.01.040.
[53] E.L.I. Ringdalen, Changes in Quartz During Heating and the Possible Effects on Si Production, JOM 67 (2015) 484–492, https://doi.org/10.1007/s11837-014-1149-y.
[54] C. Rodriguez-navarro, A. Luque, A.B. Rodriguez-navarro, Thermal decomposition of calcite: Mechanisms of formation and textural evolution of CaO nanocrystals, Am. Miner. 94 (2009) 578–593, https://doi.org/10.2138/am.2009.3021.
[55] Y. Luna-Galiano, A. Cornejo, C. Leiva, L.F. Vilches, C. Fernández-Pereira, Properties of fly ash and metakaolin based geopolymer panels under fire resistance tests, Mater. ConstrucciónN. 65 (2015) e059, https://doi.org/10.3989/mc.2015.06114.
[56] A. Fernández-Jiménez, J.Y. Pastor, A. Martín, A. Palomo, High-Temperature Resistance in Alkali-Activated Cement, J. Am. Ceram. Soc. 93 (2010) 3411–3417, https://doi.org/10.1111/j.1551-2916.2010.03887.x.
[57] P. Duxson, A. Fernandez-Jimenez, J.L. Provis, G.C. Lukey, A. Palomo, J.S.J. van Deventer, Geopolymer technology: the current state of the art, J. Mater. Sci. 42 (2007) 2917–2933, https://doi.org/10.1007/s10853-006-0637-z.
[58] C. Cao, X. Lv, H. Li, S. Wu, J. Lv, Thermal and chemical resistance of fly ash and blast furnace slag alkali-activated pastes after exposure to high temperature and NaOH, Constr. Build. Mater. 490 (2025) 142397, https://doi.org/10.1016/j.conbuildmat.2025.142397.
[59] P.C. Hewlett (Ed.), Lea's Chemistry of Cement and Concrete, 4th ed., Butterworth-Heinemann, Oxford, UK, 1998.
[60] P. Yang, T. Krevaikas, Experimental and analytical investigation of the tensile mechanism of textile-reinforced mortar (TRM) composites and fabric grids in elevated temperatures, Constr. Build. Mater. 431 (2024) 136495, https://doi.org/10.1016/j.conbuildmat.2024.136495.
[61] K. Laoubi, Z. Hamadi, A.A. Benyahia, A. Serier, Z. Azari, Thermal behavior of E-glass fiber-reinforced unsaturated polyester composites, Compos Part B 56 (2014) 520–526, https://doi.org/10.1016/j.compositesb.2013.08.085.
[62] T. Bhat, D. Fortomaris, E. Kandare, A.P. Mouritz, Properties of thermally recycled basalt fibres and basalt fibre composites, J. Mater. Sci. 53 (2018) 1933–1944, https://doi.org/10.1007/s10853-017-1672-7.
[63] P. Yang, T. Krevaikas, Residual Properties of Fibre Grids Embedded in Cementitious, Buildings 13 (2023) 1900, https://doi.org/10.3390/buildings13081900.
[64] P. Kapsalis, C. Papanicolaou, T. Triantafillou, Residual performance of alkali-activated TRM after exposure to high temperatures. 11th Int. Conf. Fiber-Reinforced Polym. FRP Compos. Civ. Eng, CICE 2023, 2023, pp. 1–12, https://doi.org/10.5281/zenodo.8108907.
[65] A. Milling, G. Amato, S. Emerson, L. Rea, S. Taylor, Tensile mechanical response of basalt TRM composites exposed to elevated temperatures, Civ. Eng. Res. Irel. 2024 Conf. Proc. (2024) 564–569.